



# 1 **Development of high-resolution multi-scale modelling system** 2 **for simulation of coastal-fluvial urban flooding**

3 Agnieszka Indiana Olbert<sup>1</sup>, Joanne Comer<sup>1</sup>, Stephen Nash<sup>1</sup>, Michael Hartnett<sup>1</sup>

4 <sup>1</sup>Civil Engineering, College of Engineering and Informatics, Ryan Institute, National University of Ireland,  
5 Galway, University Road, Galway, Ireland

6 *Correspondence to:* Dr. Agnieszka Indiana Olbert (indiana.olbert@nuigalway.ie)

7

8 **Abstract.** Urban developments in coastal zones are often exposed to natural hazards such as flooding. In this  
9 research, a state-of-the-art, multi-scale nested flood (MSN\_Flood) model is applied to simulate complex coastal-  
10 fluvial urban flooding due to combined effects of tides, surges and river discharges. Cork City on Ireland's  
11 southwest coast is a study case. The flood modelling system comprises of a cascade of four dynamically linked  
12 models that resolve the hydrodynamics of Cork Harbour and/or its sub region at four scales 90m, 30m, 6m and  
13 2m.

14 Results demonstrate that the internalisation of the nested boundary through a use of ghost cells combined with a  
15 tailored adaptive interpolation technique creates a highly dynamic moving boundary that permits flooding and  
16 drying of the nested boundary. This novel feature of MSN\_Flood provides a high degree of choice regarding the  
17 location of the boundaries to the nested domain and therefore flexibility in model application. The nested  
18 MSN\_Flood model through dynamic downscaling facilitates significant improvements in accuracy of model  
19 output without incurring the computational expense of high spatial resolution over the entire model domain. The  
20 urban flood model provides full characteristics of water levels and flow regimes necessary for flood hazard  
21 identification and flood risk assessment.

22

23

24 **Keywords:** Urban flooding; Coastal flooding; Fluvial flooding; Hydrodynamic modelling; Nesting; Moving  
25 boundary

26

27

28



29 **1 Introduction**

30 Low lying developments in coastal zones are exposed to natural hazards such as storm surges, waves, tsunamis  
31 and/or high river flows which can lead to significant flooding. Coastal flooding can result in substantial  
32 economic and social impacts including loss of life, damage to property and disruption of essential services  
33 (Brown et al. 2007).

34 Coastal flooding results from a rise of sea water level above normal predicted tide level. On the European  
35 Continental Shelf, coastal flooding is associated with storms generated in the Atlantic Ocean that travel through,  
36 or in proximity to, the shelf. Storm surges are important consequences of these storms – a temporary water setup  
37 resulting from synoptic variation of atmospheric pressure and strong winds blowing towards the shelf causing  
38 water to pile up against the coast. Surge physics is well understood in principle (Ponte, 1994); the mechanism of  
39 its propagation on the European continental shelf as a response to meteorological conditions (wind stress and  
40 atmospheric pressure signal separate) has been explained by Olbert and Hartnett (2010).

41 Flood dynamics due to a combination of multiple process drivers such as tides, surges and river inflows and  
42 their interactions is extremely difficult to understand using non-modelling methods (Robins et al, 2011). In  
43 recent years the amount of flood modelling work has risen dramatically. Yet the modelling still encounters  
44 various problems of which input data such as topography (Mason et al, 2007; Smith, 2002), mesh resolution  
45 (Sanders et al, 2010; Fewtrell, 2011; Horritt et al, 2006; Yu and Lane, 2006), bottom roughness (Mason et al.,  
46 2003; Horritt, 2000) or modelling framework (Hunter et al., 2008) are of greatest challenge. So far, one of the  
47 main issues hampering research into coastal flood modelling has been the lack of topographic data of  
48 sufficiently high resolution and accuracy along with highly resolvable efficient models. In the past decade, high  
49 resolution topographic has become more available with airborne scanning laser altimetry (LIDAR) technology  
50 (Gomes-Pereira and Wicherson, 1999) providing high resolution digital surface maps that can be used as model  
51 bathymetry (Marks and Bates, 2000). Although there are still problems with mapping urban areas and  
52 considerable post-processing is necessary to extract digital terrain model from digital surface model (Mason at  
53 al., 2007), the hydraulic/hydrodynamic models developed using LIDAR data allow them to numerically  
54 propagate surge and tidal waves into coastal areas. Model accuracy and computational cost are still issues to be  
55 addressed.

56 The most common and simple approach to the modelling of coastal flooding in urban areas is to link (externally  
57 or dynamically) longitudinal 1D or latterly averaged 2D hydraulic models with coastal models (e.g. Formaggia,  
58 2001; Chen, 2007; Brown et al., 2007). Such a set up has two significant drawbacks. Firstly, 1D/2D hydraulic



59 models work with the assumption that the lateral variations in velocity magnitudes are small, while in reality  
60 many coastal floodplains (e.g. urban areas) contain channels that have a significant influence on the  
61 development of inundation by providing routes along which storm surges propagate inland (Bates et al., 2005)  
62 and therefore may lead to misrepresentation of localized flooding (Cook and Merwade, 2009; Mark et al, 2004).  
63 Secondly, numerical errors may be introduced when linking different models with different dimensions resulting  
64 from poor conservation of momentum (Yang et al., 2012). There is evidence of proven difficulty in ensuring  
65 that each model interprets the model inputs and boundary conditions in the same way (Hunter et al. 2008;  
66 Pender and Neelz, 2010).

67 These problems may be overcome by application of a single hydrodynamic model to both coastal waters and  
68 coastal floodplains. Although such a model would allow smooth transition of the model solution between  
69 coastal waters and floodplains, the full solution at scales appropriate for flood inundation would incur a  
70 significant computational cost. On one hand, such models need to extend far enough offshore to capture the  
71 development and propagation of surge and to resolve the nonlinear shallow water dynamics (interactions  
72 between tides, surges and waves) at a resolution that is commensurate with flow features. On the other hand the  
73 model needs to include upstream river channels, tidal flats, low-lying land and urban areas which are susceptible  
74 to flooding at very fine resolution. This often results in a model setup that requires a large computational domain  
75 of which the area of particular interest (such as floodplains here) comprises only a small percentage. For  
76 structured grid models such requirements are often cost prohibitive and the alternative is to use lower resolution  
77 at the expense of accuracy. This means that model discretization is performed at scales well below those  
78 achievable with LIDAR data (the level of individual buildings in the case of urban flooding) meaning the  
79 highly-resolved LIDAR data are not being optimally used (McMillian and Brasington, 2007). Some quite  
80 successful attempts have been made using unstructured-grid models allowing selective grid refinement (e.g.  
81 Yang et al. 2012; Robins et al., 2011); however, the computational demand of these models is high. A relatively  
82 new approach to address this problem in high-resolution flood modelling makes use of continuing advances in  
83 computational resources through numerical domain decomposition and multi core architecture runs (Sanders et  
84 al., 2010). This method, however, requires substantial computational resources not commonly available yet.

85 In reality the modelling of coastal flooding (particularly in an urban environment) is a multi-scale problem that  
86 requires accurate solution at various scales ranging from coastal sea or estuary scale down to a dense street  
87 network of the inundated urban area. In the case of single rectilinear grid models, which are still the most  
88 commonly used hydrodynamic models, this spatial resolution problem may be overcome by grid nesting; this



89 involves embedding higher resolution grids within a lower resolution global large-scale grid model. Such a  
90 solution allows users to specify high resolution in a sub-region of the model domain without incurring the  
91 computational expense of fine resolution over the entire domain. Nonetheless, the nested model for simulation  
92 of floodplains must be very carefully chosen due to the flooding and drying properties of such zones; most  
93 nested models developed to date do not incorporate flooding and drying as they have been developed  
94 specifically for large-scale application where this phenomenon is not important (e.g. ROMS, Haidvogel et al.,  
95 2008) or, even if they incorporate flooding and drying such as Mike21 (DHI Software, 2001) flooding and  
96 drying of open boundaries is prohibited. This problem has been recently resolved in the multi-scale nested flood  
97 (MSN\_Flood) model of Nash and Hartnett (2010) which allows flooding and drying both within the domain and  
98 along boundaries, while maintaining accuracy and computational efficiency. This model is ideally suited for  
99 high-resolution modelling of urban flooding and, therefore, has been adopted for further development in this  
100 research.

101 In this context, the authors present in this paper for the first time the application of the state-of-the-art flood  
102 model, MSN\_Flood, to complex coastal-fluvial urban flooding in the estuary-lying Cork City which is subject to  
103 the combined effects of tides, surges and river discharges. The primary objectives of this paper then are to  
104 present the development of this model and to critically examine its capability to forecast/hindcast the urban  
105 inundation. It will be demonstrated in this paper that through the novel solution to the nested boundary, the so-  
106 called moving boundary, the nested model allows simulation of the propagation of open sea conditions up to the  
107 tidally active river upstream as well as rural and urban floodplains in a computationally efficient manner without  
108 compromising model accuracy or stability.

109 The modelling framework proposed in this research comprises of a cascade of multiple nested models that  
110 dynamically downscale large scale, coastal sea processes to the fine resolution scale of urban environments.  
111 MSN\_Flood was applied to the area of Cork City, Ireland, and its coastal floodplains; Cork City is frequently  
112 subject to coastal-fluvial flooding. An extreme flood event of November 2009 that resulted in approximately  
113 €100 million of flood damage in the city and its surrounds was chosen as a test case. The main features of this  
114 accurate and efficient hydraulic modelling are illustrated through the Cork City application. In particular,  
115 wetting and drying routine, computational efficiency and accuracy of simulated water elevations and velocity  
116 fields are subject to in-depth analysis in this research.

117 This paper is organized as follows: section 1 describes the motivation for this research and related work; section  
118 2 describes modelling, model setup and datasets; section 3 presents and compares numerical model results with



119 observed datasets; section 4 discusses the advantages the MSN\_Flood modelling system, and finally section 5  
120 contains conclusions from the research.

121

## 122 **2 Methodology**

123 In this section a modelling system for coastal flood inundation is described along with the datasets and model  
124 setup for the Cork City flood event.

125

### 126 **2.1 Modelling framework**

127 Many flood inundation events in urban environments have been modelled using simple hydraulic models (such  
128 as HEC-RAS (Pappenberger et al. 2005) or LISFLOOD-FP (Bates and De Roo (2000)) incapable of simulating  
129 flood water velocities required for accurate determination of flood wave propagation routes and assessment of  
130 risks associated with a certain flood flow magnitude. A more realistic analysis can be achieved using a  
131 hydrodynamic model that resolves both the continuity and momentum equations throughout the entire domain.

132 Here, the MSN\_Flood model was applied to Cork City using a cascade of four nested grids to describe  
133 hydrodynamics at various scales with particular interest in water elevations and velocity fields over the  
134 inundated area. This nested model facilitates the refinement of spatial resolution in Cork Harbour from 90 m at  
135 the outer reaches of the harbour down to 2 m in the streets of Cork City.

136

### 137 **2.2 Hydrodynamics**

138 MSN is a two-dimensional, depth-averaged, finite difference model and its solver is based on the alternate  
139 direction implicit (ADI) solver developed by Falconer (1984) (Lin and Falconer, 1997, Nash and Hartnett,  
140 2010). The governing differential equations used in the model to determine the water elevation and depth  
141 integrated velocity fields in the horizontal plane are based on integrating the three-dimensional continuity and  
142 Navier-Stokes equations over the water column depth. Assuming vertical accelerations are negligible compared  
143 with gravity and that the Reynolds stresses in the vertical plane can be represented by a Boussinesq  
144 approximation, then the depth integrated continuity and x-direction momentum equations are of the following  
145 form (Falconer and Chen, 1991):

146

147

148



149 Continuity equation

$$150 \quad \frac{\partial \zeta}{\partial t} + \frac{\partial q_x}{\partial x} + \frac{\partial q_y}{\partial y} = 0 \quad (1)$$

151

152 Momentum equation in x-direction

$$153 \quad \frac{\partial q_x}{\partial t} + \beta \left[ \frac{\partial U q_x}{\partial x} + \frac{\partial U q_y}{\partial y} \right] = f q_y - g H \frac{\partial \zeta}{\partial x} + \frac{\rho_a C^* W_x (W_x^2 + W_y^2)^{1/2}}{\rho} \quad (2)$$

154

$$155 \quad - \frac{g U (U^2 + V^2)^{1/2}}{C^2} + 2 \frac{\partial}{\partial x} \left[ \varepsilon H \frac{\partial U}{\partial x} \right] + \frac{\partial}{\partial y} \left[ \varepsilon H \left[ \frac{\partial U}{\partial y} + \frac{\partial V}{\partial x} \right] \right]$$

156 where,  $t$  = time

157  $q_x, q_y$  = depth integrated volumetric flux components in the x,y directions

158 ( $q_x = UH, q_y = VH$ )

159  $H$  = total water depth

160  $\beta$  = momentum correction factor for non-uniform vertical velocity profile

161  $f$  = Coriolis parameter ( $= 2\omega \sin \phi$ , where  $\omega$  = angular velocity of the earth's rotation and  $\phi$  =  
 162 geographical latitude)

163  $g$  = gravitational acceleration

164  $\rho_a, \rho$  = air and fluid densities respectively

165  $C^*$  = air-water interfacial resistance coefficient

166  $W_x, W_y$  = wind velocity components in x,y directions

167  $C$  = Chezy bed roughness coefficient

168  $\varepsilon$  = depth mean eddy viscosity

169

170

### 171 2.3 Nesting structure and procedure

172 MSN\_Flood consists of one outer coarse grid called the parent grid (PG) into which one or more inner fine grids

173 (child grids, CG) are one-way nested. The model also enables multiple nesting such that a child grid may also be



174 a parent to another child. In this way, multi-scale nesting can be specified enabling high spatial resolution in  
 175 areas of interest. PG and CG models are dynamically coupled and synchronous. An overview of the nesting  
 176 procedure is schematically presented in Fig. 1. As can be seen, the time integration is a bottom-up approach  
 177 where PG can be advanced in time only when all of its children are integrated to the parent current time. The  
 178 ADI solution technique to solve the governing continuity and momentum equations requires the sub-division of  
 179 each timestep into two half-timesteps. The nesting procedure, for each nesting level, is summarized in the  
 180 following 5 steps:

- 181 1. integrate outermost parent grid one timestep ( $t+\Delta t_p$ )
- 182 2. extract parent grid data and interpolate (spatially and temporally) along child grid boundary to next time  
 183 levels of child grid ( $t+\frac{1}{2}\Delta t_c$ ) and ( $t+\Delta t_c$ )
- 184 3. integrate child grid one timestep ( $t+\Delta t_c$ )
- 185 4. repeat Steps 2 and 3 so that the child grid is synchronised to the current timestep of parent grid ( $t+\Delta t_p$ )
- 186 5. return to Step 1 and continue.

187 The nesting procedure is similar in principle to other nested models (Holt et al., 2009; Korres and Lascaratos,  
 188 2003; Nittis et al., 2006) but the uniqueness of MSN\_Flood is a novel approach to boundary formulation  
 189 through an incorporation of ghost cells in a manner that the nested boundary operates as an internal boundary.  
 190 Ghost cells (GC) are specified adjacent to nested boundaries so that the boundary configuration consist of two  
 191 rows/columns of CG cells: internal boundary cells and the adjacent exterior ghost cells. A schematic of the  
 192 general configuration of the nested boundary is shown in Fig. 2. In this internal boundary approach, PG  
 193 boundary data is specified to both the ghost cells outside the CG domain and to the internal boundary cells  
 194 allowing the governing equations of motion at the internal boundary grid cells to be formulated and solved in  
 195 the same way as interior grid cells. This enables accurate specification and conservation of incoming fluxes of  
 196 mass and momentum along the boundaries of the nests. To demonstrate benefits of this approach the finite  
 197 difference formulation for the advective term in the momentum equation, which is key to momentum  
 198 conservation, at boundary cells becomes:

199

$$200 \frac{\partial U q_x}{\partial x} = \left[ \frac{[U(x+\Delta x, y)+U(x, y)]}{2} \cdot \frac{[q_x(x+\Delta x, y)+q_x(x, y)]}{2} \right. \quad (3)$$

$$201 \left. - \frac{[U(x, y)+U(x-\Delta x, y)]}{2} \cdot \frac{[q_x(x, y)+q_x(x-\Delta x, y)]}{2} \right]$$



202 For comparison, in a boundary formulation without ghost cells, the derivative  $\partial U_{q_x} / \partial x$  would be set to zero  
203 as ghost cell grid points  $U(x + \Delta x, y)$  or  $U(x - \Delta x, y)$  would not exist, therefore momentum would not be  
204 conserved between parent grid and child grid.

205 An important feature of the nesting approach in MSN\_Flood is the implementation of moving boundaries along  
206 the boundary of the nested domains. The flooding and drying routine originally developed in by Falconer and  
207 Chen (1991) is implemented in MSN\_Flood; this boundary formulation allows the model to be applied to areas  
208 of inter-tidal zone or coastal flooding where there is typically a considerable degree of alternate flooding and  
209 drying throughout the domain. The flooding and drying routine by Falconer and Chen has been extensively  
210 tested in laboratory conditions and natural waterbodies and shown to be stable and robust. However, when the  
211 nested boundary was subject to flooding and drying, despite the overall improvement in mass and momentum  
212 conservation along the nested boundary, significant errors were found to occur near the boundary in areas of  
213 flooding and drying. This problem was overcome by implementation of an adaptive interpolation scheme which  
214 uses linear interpolation or zeroth-order interpolation depending on the status (wet or dry) and the configuration  
215 of parent grids along the boundary interface. More details of the method can be found in Nash (2010). This  
216 adaptive interpolation in combination with ghost cell and internal boundary formulation ensures the stable  
217 flooding and drying of boundary cells.

218 The ghost cell formulation of the boundary was found to significantly reduce boundary formulation errors, one  
219 of three error sources in nested models as classified by Nash and Hartnett (2010). Boundary formulation errors  
220 arise from simplification of mathematical formulation of the governing equations of motion at open boundary  
221 grid cells. Two other sources of errors at the boundary interface are boundary specification errors and boundary  
222 operation errors. While the former errors arise from incorrect boundary data, and can be minimised by locating  
223 nested boundary in areas of high PG accuracy, boundary operator errors result from the use of an inadequate  
224 interpolation schemes and/or boundary condition for prescribing PG data to the CG boundary and are more  
225 challenging to reduce. During the course of model developments various interpolation schemes were tested  
226 including a zeroth order scheme, a linear scheme, a mass-conserving quadratic scheme and an inverse distance  
227 weighted scheme. The linear interpolation was found to be most accurate in both time and space and therefore  
228 was implemented in the model (Nash, 2010). With regards to the boundary conditions, three different types of  
229 boundary conditions were tested, namely: Dirichlet condition, flow relaxation condition and radiation condition.  
230 Extensive numerical testing showed that the most stable and accurate model solution could be achieved by





231 implementing the Dirichlet boundary condition. Accuracies of various interpolation and boundary condition  
232 schemes were analysed and compared in Nash and Hartnett (2014).  
233 Reduction in boundary errors due to the accurate development of boundary operators and more accurate  
234 mathematical formulation of the nested boundary yielded significant improvements in conservation of mass and  
235 momentum between parent and child grids. This in turn improved model stability at the nested boundary and  
236 CG accuracy. These features make MSN\_Flood highly applicable to modelling complex coastal flooding events  
237 as in the current test case, where the nested boundary is located in the flooding and drying zone, and therefore  
238 its length changes dynamically throughout the flooding event. This non-continuous moving boundary feature is  
239 the subject of in-depth investigation in this research.

240

241

#### 242 **2.4 Study area description and model setup**

243 Cork Harbour, in the southwest of Ireland, is a shallow (average depth 8.4 m) meso-tidal estuary with typical  
244 spring tide ranges of 4.2m. Return levels of tides for 2- and 100-year return periods are 4.45 m and 4.52 m  
245 above chart datum, respectively, while surge residual return levels for the same return periods are 0.56 m and  
246 0.85 m, respectively (Olbert and Hartnett, 2013). The Cork Harbour domain is presented in Fig. 3. Cork City is a  
247 densely populated urban area of approximately 120,000 people, located at the mouth of the River Lee which  
248 drains into Cork Harbour. Tidal components of flooding in Cork City are due to combinations of high  
249 astronomical tides and storm surges generated in the open ocean and propagating into the Harbour and  
250 throughout the city streets. The River Lee corridor flows from west to east along the post-glacial valley into the  
251 Lee proper, through Cork City, into Lough Mahon, Cork Harbour and south into Atlantic Ocean. In the city, the  
252 River Lee bifurcates into the north and south channels around the Mardyke area and merges again at the eastern  
253 edge of the city. The river flows for 2- and 100-year return periods are 208.6 and 307.7 m<sup>3</sup>/s, respectively  
254 (Halcrow 2008). Sea water intrusion up the river is bounded by a weir located 8km upstream from the river  
255 mouth.

256 MSN\_Flood was used in this research to develop a coastal-urban hydraulic model capable of simulating fluvial  
257 and coastal flooding in the Cork City. The model grid needs to be setup to include not only river channel and  
258 urban floodplains but also offshore waters necessary to resolve the non-linear hydrodynamics. The Cork  
259 Harbour/City model is therefore configured as a four level cascade of dynamically linked nested grids that  
260 resolve the hydrodynamics of the region at spatial scales of 90m, 30m, 6m and 2m. Each coarser grid provides



261 boundary conditions to the next finer grid, i.e. the 90m grid provides boundary conditions to the 30m grid and  
262 the 30 m grid provides boundary conditions to the 6m grid, etc. Fig. 4a illustrates the extent of each grid and the  
263 nesting structure, while Fig. 4b shows details of the high resolution 6m grid and the 2m urban flood grid.

264 The parent grid (PG90) representing the full domain of Cork Harbour was resolved at a grid spacing of 90m. At  
265 3:1 nesting ratio, the first child grid (CG30), completely embedded within the parent model domain, has a grid  
266 spacing of 30m. The CG30 model provides boundary conditions to a 6m grid (CG06) at a 5:1 nesting ratio. The  
267 domains of CG30 and CG06 models only partially overlap. Water elevations computed on CG30 are passed to  
268 the eastern boundary of CG06 while River Lee flow data are specified at the western boundary of CG06.  
269 Finally, the ultra-high resolution 2m child grid (CG02) is entirely embedded within CG06 and is used to  
270 simulate urban flooding of Cork City. The nesting ratios of 3:1 and 5:1 used in this setup are in line with nesting  
271 ratios used in other studies (e.g. Spall and Holland, 1991). Configurations of the nested models are summarized  
272 in Table 1.

273 Open boundary conditions to the MSN\_Flood parent grid, PG90, are provided as total water elevations  
274 containing tidal and surge signals extracted from an ocean model of the North East Atlantic (Olbert and  
275 Hartnett, 2010). The surface boundary of the MSN\_Flood model is forced by 10-m wind fields and mean sea  
276 level atmospheric pressure obtained from the regional analysis ERA-40 model (Uppala et al., 2005) and  
277 operational model first-guess dataset (Simmons et al., 1989). River Lee discharges from gauge station 19011  
278 were provided by Office of Public Works (OPW), Ireland. Admiralty Chart data were used to develop the  
279 bathymetric model of Cork Harbour, while high resolution LiDAR data provided by the OPW were used to  
280 construct the high resolution urban digital bathymetric model. The channel of the River Lee was included in the  
281 model based on cross-sectional survey data also provided by the OPW from an extensive survey of the River  
282 Lee catchment in 2008.

283

### 284 **3 Results**

285 Showcasing the capability of the multilevel nesting integrated system to accurately simulate the extent and level  
286 of urban flooding is central to this research. MSN\_Flood has been extensively tested in both laboratory settings  
287 (against physical tidal models) and natural open harbours. In this research, a comprehensive validation of the  
288 model in a coastal flood application to Cork Harbour and the urban environment of Cork City is presented.  
289 Initial evaluation of model accuracy is carried out at each of the four levels of nesting; both modelled water  
290 elevations and velocities are compared to available field data. The assessment of the model skill in simulation of



291 urban flooding is carried out for the November 2009 coastal-fluvial flooding of Cork City. In this application,  
292 the city streets and open areas are treated as hydraulics channels and plains that can be inundated depending on  
293 the tide, surge and fluvial conditions. This is a highly complex hydrodynamic region to model and, therefore,  
294 represents a robust test of the model.

295

296

### 297 3.1 Validation of the nesting procedure

#### 298 3.1.1 PG90 model

299 Firstly, the performance of the low resolution 90m parent grid (PG90) model was assessed. Figure 5 compares  
300 current velocities simulated by the PG90 model with measured data at Passage West in Cork Harbour over a  
301 spring tidal cycle (see Fig. 3 for point P1 location). Results show that although pattern of currents through flood  
302 and ebb conditions are relatively well predicted, the slack water conditions, where velocities are generally  
303 smaller, are not reproduced correctly by the PG90 model. A higher resolution single grid (SG30) model at 30m  
304 grid spacing was developed to test the accuracy of PG90. The same domain extents (Fig. 4) and the same  
305 physical conditions were specified to the SG30 and PG90 models. As shown in Fig. 5 an increased resolution of  
306 the model significantly improves model predictions throughout the tidal cycle and particularly during periods of  
307 slack water.

308 The spatial distribution of PG model error was quantified by calculating the tidally-averaged relative errors  
309  $RE_T$  which expresses a percentage error in a PG solution,  $Y$ , relative to a higher resolution SG reference  
310 solution,  $X$ , at the output time  $n$  over a tidal cycle ( $N=25$ )

$$311 \quad RE_T = \frac{\sum_{n=1}^N |Y_n - X_n|}{\sum_{n=1}^N |X_n|} \cdot 100 \quad (4)$$

312 Figure 6 shows the distribution of  $RE_T$  in PG velocities in Cork Harbour; it can be seen that the errors generated  
313 by the PG model are well over 30% at certain locations within the harbour (harbour entrance, along the  
314 coastline, narrow channels and estuaries) so increasing the resolution from 90m to 30m leads to significant  
315 reduction in the error. However, improvements in accuracy due to higher spatial resolution come at a high  
316 computational cost which for the SG model (80min for 50hrs run) is nine times that of the PG model (9min for  
317 50 hrs run). The use of nested model is then a justifiable and favourable solution.



318 In the course of extensive validation, the timeseries of PG90 and SG30 were also inter-compared. Figure 7  
319 shows water elevations and current velocities in Lough Mahon (see Fig. 3 for point C1 location). Water  
320 elevations computed by both models are in very good agreement. In contrast, current velocities are significantly  
321 overpredicted by the PG90 model. Linear regression of current speeds of PG90 against SG30 solution is shown  
322 in Fig. 8. As can be seen from this figure the correlation coefficient between PG90 and SG30 is 0.89 while slope  
323 and intercept are  $m=1.24$  and  $c=0.03$ , respectively.

324

### 325 3.1.2 CG30 model

326 The selection of a child grid domain configuration is sensitive to the location of boundaries that may affect the  
327 overall stability and performance of the nested model solution. Suitable CG boundaries must be located in areas  
328 of low PG inaccuracy and at a sufficient distance from the area of interest as location of the boundary close to  
329 the area of interest may result in boundary errors propagating into the area causing the accuracy of the solution  
330 to deteriorate. On the other hand, boundaries need to be sufficiently close to the area of interest in order to  
331 minimize the domain size (computational cost).

332 The first level child grid, CG30, was located in the north-west part of Cork Harbour with the centrally located  
333 Lough Mahon (directly feeding to the River Lee estuary) being the area of interest. The boundaries for the CG30  
334 domain were chosen based on the  $RE_T$  distribution plot for the PG90 current velocities presented in Fig. 6. The  
335 upper section of Passage West, connecting Lough Mahon with Lower Harbour, was selected as a suitable  
336 southern boundary (SB) due to its relatively low  $RE_T$  while the closest suitable location for the eastern  
337 boundary (EB) was at a much greater distance from Lough Mahon due to generally high PG inaccuracies in the  
338 North Channel.

339 The accuracy of the CG30 boundary location was assessed by comparing the net fluxes of mass and momentum  
340 across the corresponding interfaces in the PG90, SG30 and CG30 models. Net fluxes were calculated normal to  
341 boundaries. Mass and momentum fluxes through the SB and EB boundaries are compared in Fig. 9 and 10,  
342 respectively. It can be seen that the predominant forcing-boundary for the CG30 domain is the SB boundary.  
343 The tidally-averaged errors in PG90 fluxes relative to the SG30 were approximately 4% for both mass and  
344 momentum indicating a high level of PG90 accuracy. At the EB boundary, the PG90 accuracy was slightly  
345 lower resulting in error in PG90 mass flux of 5% and momentum flux of 10%. However, this boundary  
346 accounted for a smaller portion of the total boundary forcing, and its distant location from the area of interest  
347 allowed boundary errors more time to dissipate. The tidally-averaged errors in CG30 fluxes (both mass and



348 momentum) relative to PG90 fluxes were less than 2% at both boundaries, demonstrating high levels of  
349 conservation from parent grid to child grid.

350 Relative error analysis was also carried out for the entire CG30 model domain with respect to water elevations  
351 and velocities, and results of these analyses are summarized in Table 2. The domain-averaged relative error  
352  $RE_D (= RE_T / N)$  in the PG90 water elevations relative to the SG30 were 5.9% while in the CG30 model  
353 this error was reduced to 1.1%. The extent of the domains with  $RE_T$  greater than 1% was 94% for PG90 and  
354 28% for CG30. The absolute error defined as:

$$355 \quad AE_T = \frac{\sum_{n=1}^N |Y_n - X_n|}{N} \quad (5)$$

356 was also calculated.  $AE_T$  in water level significantly decreased from 8cm in the PG90 to 1.2 cm in the CG30.  
357 In relation to current velocities, the  $RE_D$  was reduced from a large value of 22.4% in PG90 to just 0.5% in  
358 CG30; while  $RE_T$  values exceeding 5% were found in 72% and 4% of the PG90 and CG30 domains,  
359 respectively.

360 As shown in Fig. 7, timeseries of water elevations and current speed show very good agreement between SG30  
361 and CG30 throughout the tidal cycle. This indicates significant improvement in the accuracy of velocity  
362 computation using the high resolution nested CG30 and is verified by the linear regression analysis shown in  
363 Fig. 8. The superiority of CG30 over PG90 model when compared to SG30 is clear and confirmed by a  
364 correlation coefficient of 0.99 compared to 0.89. The slope and intercept were also improved for CG30 when  
365 compared to PG90; with  $m=1.01$  and  $c=-0.01$  the CG30 against SG30 model solutions lie approximately on the  
366 45° line.

367 These results demonstrate that the application of the nested high resolution model results in significant  
368 improvement in the accuracy of the model solution over the lower resolution PG solution. Similar to the  
369 improvement in model accuracy, an equally significant reduction in computational effort was achieved. For  
370 example, the application of MSN\_Flood model to level 1 domain nesting yields 21 minutes simulation time for  
371 the PG90-CG30 model; this is contrasted by 80 minutes simulation time for the SG30 model. Thus the nested  
372 model runs 3.8 times quicker than the single grid model.

373

374



### 375 3.1.3 CG06 model

376 In contrast to the CG30 grid being fully embedded within the PG90 grid, in the second level of nesting CG06 is  
377 only partially nested within its parent CG30 (Fig. 4). Approximately 38% of wet cells in CG06 overlap CG30.

378 This is a hybrid boundary structure where the east boundary is prescribed using hydrodynamic data from the  
379 parent model while the west boundary is prescribed using measured data. The west boundary is a flow  
380 boundary, with River Lee inflows extracted from river gauging station 19011. The east boundary is a water  
381 elevation boundary where water elevations are supplied along the boundary by the CG30 model. The location of  
382 the latter boundary was selected to correspond to the position of the Tivoli tidal gauge station and therefore to  
383 contribute to model validation (see Fig. 3 for location of Tivoli gauge).

384 Validation of the CG06 model is conducted for the flood event of November 2009, which due to a combination  
385 of heavy river discharges and high tides coinciding with moderate surges resulted in extensive inundation of the  
386 area delineated by this nested grid. Figure 11 compares timeseries of water elevation computed at the CG30-  
387 CG06 nested boundary (east boundary) against tidal gauge records from the same location. Overall, there is a  
388 very good agreement between predicted water elevations and measured data. The high degree of model accuracy  
389 is manifested by high correlation (0.992) and a low value of RMS difference (0.022m) shown in Table 3 (model  
390 CG06\_1). Both the RMSE (0.142m) and centred RMSD (0.141m) indicate that the model is able to reproduce  
391 variability of water elevation with a good accuracy (order 0.14m). Further, a small difference between these two  
392 statistical measures implies that the mean values of observations and simulation are very close. Interestingly, the  
393 accuracy of the CG06 model is improved when a 6 minutes phase shift (one record timestep) between  
394 observations and simulation is artificially introduced (model CG06\_2 in Table 3). This results in RMSE  
395 (RMSD) reduction to 0.106m (0.104m) and an increase of correlation to 0.996. It is deemed then that there is a  
396 phase lag between model and observations of approximately one observational timestep. Another aspect of the  
397 analysis involved temporal occurrence of an error. As the model-observations discrepancies are observed around  
398 low water levels (which is not so significant to this study), by not considering negative water elevations (below  
399 0 mOD Malin) the RMSE is further reduced to 0.075m (model CG06\_3 in Table 3). Such level of agreement  
400 between model and observation is considered to be satisfactory.

401 The effect of horizontal resolution on model skill is also examined. This is carried out by comparing the model  
402 performance at 6 m and 2m resolutions. For this purpose a single grid 2m reference model (SG02) covering the  
403 area delineated by the CG06 model was developed. Figure 12 presents the distribution of water level  $RE_T$  in  
404 the CG06 solution relative to the SG02 reference solution. In general, errors in CG06 outside the Cork City



405 centre are very low (<10%) implying that flooding in the rural area of Cork is well resolved using the 6m grid.  
406 In contrast, significantly higher errors are obtained in the Cork City (CG02 domain), and in particularly in areas  
407 of narrow dense streets where errors exceed 30%. Here, an increase in model resolution leads to a significant  
408 reduction in errors. This implies that next level of nesting is required to improve the model accuracy in the city  
409 centre.

410

#### 411 3.1.4 CG02 model

412 Finally, the highest resolution 2m model (CG02), fully embedded within CG06, covers the urban area of Cork  
413 City; this area is particularly prone to flooding. In the first step of model skill analysis, water elevations  
414 simulated by the CG06 and CG02 models at four locations along the river channel are compared in Fig. 13 and  
415 statistically summarized in Table 4. Again, the November 2009 flood event was used as a benchmark. Close to  
416 the east boundary, at point CG02\_4 (see Fig. 14 for point location), both models perform almost identical and  
417 this is visually and statistically confirmed in Fig. 13d and in Table 4, respectively. Discrepancies between the  
418 CG06 and CG02 models increase with distance from the nested east boundary and are manifested by overall  
419 higher water elevations computed by the coarser CG06 model. Location CG02\_2 (Fig. 13b) shows the biggest  
420 discrepancy evidenced by the statistical measures RMSE=0.195m, RMSD=0.109m, RMSdiff=-0.181m. Despite  
421 overprediction of water elevations by the CG06 model, the general water level trends in the two models are in  
422 good agreement (COR=0.997). Another important advantage of a high resolution model is an improved  
423 numerical stability of the model solution. As can be seen from Fig. 13 a-c, some infrequent random oscillations  
424 in water levels occurring in CG06 from numerical instability due to insufficient grid resolution are not present in  
425 the finer CG02 model.

426 The effect of improved horizontal resolution is analysed spatially by means of  $RE_T$  distribution plots. As  
427 shown in Fig. 12, the 2m resolution is essential to resolve small scale processes of complex urban area. Figure  
428 14 compares  $RE_T$  between CG02 and SG02. In general,  $RE_T$  is quite low at 10% in the western part of the  
429 city along river banks increasing in eastward direction to 20% in narrow streets of city centre. This is a  
430 considerable improvement when compared to  $RE_T$  in CG06 relative to SG02. Moreover, as CG02 achieves a  
431 similar level of accuracy to SG02 the computational cost is significantly reduced and constitutes enormous 96%  
432 saving.



433 From this analysis it can be seen that the CG06-CG02 nesting results in a model performance generally  
434 comparable to the single grid SG02 model but at a significantly reduced computational cost when compared to  
435 the single grid model.

436 The ultimate conclusion from the model validation is that MSN\_Flood facilitates significant improvements in  
437 model accuracy without incurring the computational expense of high spatial resolution over the entire model  
438 domain. The model setup constitutes a rigorous test of model performance and on that basis it can be further  
439 concluded that the model is applicable to situations where nested boundaries are located in complex urban  
440 floodplains that periodically wet and dry.

441

### 442 **3.2 Urban flood modelling**

443 For most of the time, city streets are dry and rivers draining the hinterland are contained within well-defined  
444 river banks or walls. However, when extreme flood events occur rivers may burst their banks and the city  
445 streets become water conveyance channels. The simulation of the hydrodynamics associated with rapid urban  
446 flood events is complex; many significant issues must be addressed such as flooding and drying, spatial  
447 resolution, domain definition, frictional resistance and boundary descriptions. When modelling flood events, the  
448 mathematical formulation of the nested boundaries that permit flooding and drying is of particular importance.  
449 Also, the horizontal resolution necessary to resolve small scale processes must be considered. In particular,  
450 these aspects of the MSN\_Flood model will be discussed in this section.

451

#### 452 **3.2.1 Extreme flood event**

453 On the 19<sup>th</sup> and 20<sup>th</sup> of November 2009 high River Lee flows combined with high astronomical tides and  
454 moderate surge caused localized overtopping/breaching of the river banks resulting in widespread flooding of  
455 Cork City. Evolution of the flood wave propagation simulated by the CG02 model is shown in Fig. 15.  
456 Maximum flooding was reached at 9:30 on 20/11/2009 around the time of high tide and approximately 5 hours  
457 after peak discharge of River Lee. At this juncture over 62ha of Cork City had been flooded. The most affected  
458 zone was the city centre located between the north and south channels of the river; this area is a low-lying island  
459 that over centuries was gradually reclaimed from marshland and its low-lying topography combined with the  
460 influence of river, estuary and harbour makes the area particularly vulnerable to flooding.

461 The accuracy of the urban inundation simulation was assessed against field observations of inundation extent  
462 and maximum heights of flood waters. The observed and modelled ultimate extents of flooding in the city are





463 shown in the Fig. 16; the hindcasted extent of inundation matches very well that observed during the flood  
464 event. With regards to flood level heights, observed water level marks were collected and post-processed by  
465 OPW at 38 survey points across the flooded area; their distribution is shown in Fig. 17. The survey point data  
466 were subsequently used to calibrate the model. Initial calibration tests showed that the model was most sensitive  
467 to bottom roughness coefficient. An extensive statistical analysis of bed roughness parameterization was used to  
468 provide an accurate model solution for flood inundation; details of that analysis are presented elsewhere. The  
469 best fitting results ( $R=0.97$ ,  $RMSD=0.26$ ) were obtained for the following roughness values: upper  
470 channel=0.90, lower channel=0.90, roads=0.1, city floodplain=0.1 and upstream floodplain=0.30. Figure 18  
471 provides visual assessment of the best fit model skill; good agreement between the model and observations is  
472 achieved as the model solution falls on the  $45^\circ$  line. Interestingly, better agreement was found for survey  
473 locations in floodplains as opposed to points adjacent to the river bank. This could be attributed to the fact that  
474 the majority of survey points are located away from the channel edge (many are actually at the floodplain edge).

475

### 476 3.3 Moving boundary

477 The specification of a nested boundary in a flood-prone area is particularly problematic; nested models  
478 developed so far prohibit flooding and drying along open boundaries. This problem has been overcome in  
479 MSN\_Flood; its unique mathematical formulation of the nested boundary involving ghost cells, internal  
480 boundary formulation and adaptive interpolation, ensures stable flooding and drying of boundary cells. In  
481 MSN\_Flood, any nested boundary can be placed within a flooding and drying zone and therefore may be subject  
482 to significant lateral expansion and contraction. Moreover, the internalization of the boundary allows the  
483 flooding and drying mechanism to approach the boundary of the nested domain from either upstream or  
484 downstream. As the boundary alternatively floods or dries, the number of active boundary cells expands and  
485 contracts accordingly. Depending on local topography, not only the length of the boundary may change but also  
486 the number of active boundaries changes. Such a boundary is therefore a complex, non-continuous, moving  
487 boundary that spatially and temporally changes its characteristics. This is a significant aspect of this research.

488 In the model setup, the urban CG02 model is entirely embedded within the CG06 model; mass and momentum  
489 from the 6m model is transferred to the 2 m model via two nested boundaries – the western boundary  
490 transferring River Lee waters from the upper to the lower channel of the river (it also geographically divides the  
491 floodplains into upper and lower floodplains), and the eastern boundary exchanging waters with the estuary. The  
492 western boundary of CG02 is located on the upstream fluvial floodplain which is prone to wetting and drying. A



493 cross section through this boundary illustrating the steep gradients of the river channel bathymetry and the  
494 topography of the adjacent urban floodplains (which includes buildings) is shown in Fig. 19. The temporal  
495 progression of water levels throughout the November 2009 flooding is also plotted. The reference water level at  
496 simulation time  $t=4\text{hr}$  corresponds to a  $187\text{ m}^3/\text{s}$  river flow (19<sup>th</sup> of November 2009 at 01:30). At this juncture  
497 the flow greatly exceeds the average river flow of  $40\text{ m}^3/\text{s}$  as it results from increased discharges from Inniscarra  
498 dam. The storage capacity of Inniscarra Reservoir had been reached after a month-long period of record high  
499 rainfalls and heavy downpours on the 18<sup>th</sup> and 19<sup>th</sup> of November. Over the course of the subsequent 28 hours  
500 the discharges further increased to reach a maximum value of  $560\text{ m}^3/\text{s}$  at 2:30 on November 20<sup>th</sup>. The water  
501 level at the boundary increased from 4.57 mOD at 22:30 November 18<sup>th</sup> to a peak of 5.74 mOD 28 hours later.  
502 The extensive inundation of the upper channel floodplains (upstream floodplains) has a major effect on the  
503 western boundary of the CG02 model. It can be seen in Fig. 19 that as the flooding progresses to a simulation  
504 time of 8hrs a second wetted boundary is created south of the main channel boundary due to bifurcation of  
505 flood waters into two channels (called here the main and side channels) approximately 1.2km upstream of the  
506 boundary. Importantly, there is a significant difference in water elevation of 0.41m between the two channels of  
507 the boundary. This results from the topography of the upstream floodplains and therefore local flow conditions.  
508 The reason for the difference in water elevations along the two sections of the boundary can be explained with  
509 the help of Fig. 20 showing three cross-sections including one (cross-section 3) located close to the nested  
510 western boundary. As simulated by the CG06 model, downstream from cross-section 1, representing the  
511 maximum cross-sectional extent of the inundated area, flood waters must flow around an elevated strip of rural  
512 land and so splits at this point into two floodplain channels. This is shown in cross-section 2, located at mid  
513 length of this 1 km long strip of land; here the water elevation difference between two channels is 0.31m. This  
514 elevation difference further increases to 0.41m near the nested boundary (cross-section 3).

515 The temporal rise of water levels at a number of points across the western nested boundary is shown in Fig. 21.  
516 Series A represents the main river channel, series B and C correspond to points adjacent to the river channel  
517 while series D is located in the side channel. The difference in water elevations between the two boundaries is  
518 apparent throughout the entire flooding period, though it is reduced with the progress of flooding.

519 An interesting characteristics of the moving boundary is its change in its length. As flood waters continue  
520 overtopping the river banks, the area of inundation increases and is reflected in the elongation of the boundary.  
521 The length of the main channel boundary is initially equal to the river width, this nearly doubles during flooding



522 as shown for  $t=12$  hrs in Fig. 19. The temporal evolution of flooding through the boundary clearly demonstrates  
523 that the nested boundary is a discontinuous moving boundary with a variable head.

524 The numerical stability of such dynamically changing properties of nested boundary is an important aspect of  
525 nesting procedures. Overall, a change in length as well as division into separate subsections does not markedly  
526 impact computational stability nor model performance. In fact, as shown in Fig. 14,  $RE_T$  computed over the  
527 flooding period remain low within the CG02 domain despite significant changes to nested boundary  
528 configurations and flow conditions.

529 As demonstrated in this section MSN\_Flood is developed in a general-purpose manner that through stable and  
530 accurate moving boundary provides a high degree of choice and flexibility regarding the location of the  
531 boundaries to the nested domain.

532

### 533 3.4 Model resolution

534 Due to the highly irregular topography of urban environments and the highly dynamic flows involved, urban  
535 flooding is a complex problem. Most of the flood models developed so far have focused on rural or semi  
536 developed floodplains where isolated large structures can be modelled while small objects are ignored or  
537 parameterized as bottom friction (Brown et al., 2007). Such modelling does not implicitly account for locking  
538 effects of building on flow. As the presence of buildings may substantially increase flood extent when compared  
539 with undeveloped floodplains the role of high resolution discretization is paramount. However, as Brown et al.,  
540 (2007) found, the greatest source of modelling error with respect to grid resolution is associated with the  
541 steepest gradients in topography which are susceptible to interpolation error.

542 Modelling of flood flow through urban area is difficult because of its need for stable and accurate solution of the  
543 flow equation (Brown et al., 2007). Since accurate modelling requires a resolution commensurate with flow  
544 features, dense street network flows through urban floodplains can only be fully resolved with a sufficiently  
545 high resolution. However, satisfactory model resolution, and thus accuracy, incurs computational expense; a  
546 balance between these two contradicting factors provides an optimal solution. Gallegos et al. (2009) found that a  
547 5m resolution mesh that spans a street by approximately three cells achieves such balance. The characteristics of  
548 urban residential areas of southern Californian investigated in their study is different than that of an old  
549 European development type towns comprising of narrow dense streets as Cork City. It follows that the 5m  
550 model resolution is insufficient to resolve flow dynamics in such city centre street networks.



551 In order to analyse the overall effect of model resolution on simulation results, CG06 and CG02 model results  
552 are compared. Visual comparison of flood inundation can be made from Fig. 22 which shows CG06 and CG02  
553 model outputs representing the maximum extent of inundation during the November 2009 flooding. There is a  
554 discrepancy in the extent and magnitude of flooding between the two models. Some zones and streets do not get  
555 flooded in the CG06 model, which may be caused by the coarse representation of the street network and  
556 associated lack of connectivity between certain streets, while in other zones flood water is present in areas  
557 which remain dry according to observations and CG02 output. Figure 23 (a) shows the difference in water  
558 elevations between CG02 and CG06 interpolated onto the 2m grid. It is clear that both the height and area of  
559 flooding are affected. The absolute difference in water level is on average 0.13m and is underestimated by the  
560 6m model by up to 0.4m in the upper section of river and overestimated by approximately 0.3m in the lower  
561 section. Figure 23 (b) shows a spatial distribution of RMSE between two models. There is a noticeable reduction  
562 in model performance at coarser resolution of 0.08m RMSE over the entire domain and the error is generally  
563 larger in the dense street network of the urbanized zone. Based on model results it is clear that a substantial  
564 portion of the error results from the coarse representation of topography since its gradient is greater than the  
565 slope in water surface; however, some small portion of the error could be attributed to errors in LIDAR data  
566 (~0.1m RMSE according to Bates et al, 2010) as well as interpolation from 6m down to 2m grid.

567 Another comparative measure involves a computation of relative differences in inundated area and flood water  
568 volume between coarse and fine grid models expressed as a following ratio

$$569 \quad RD = \frac{|X_f - X_c|}{X_f} \quad (6)$$

570 Where  $X$  is total inundated area or volume in the domain at a particular time whereas indices  $c$  and  $f$  denote  
571 CG02 and CG06 solutions, respectively.

572 Figures 24 (a) and (b) show the evolution of differences in inundated areas and volumes throughout the  
573 simulation. The significantly high relative difference in the area at the initial stage of flooding reaching 36% is  
574 misleading as the relatively small total inundated area with a small flood time lag results in large discrepancies  
575 at this stage (ca. 11ha). Nevertheless, when the flooding is more pronounced (over 30 ha, max 62.6ha) the  
576 relative difference is still up to 10%. With regards to flood water volume in inundated areas the difference is  
577 over 20% during first hours of flooding and still remains as high as 10% throughout the flood peak only falling  
578 to below 10% when the flood recedes. The total RMSE of inundated area and volume between 2m and 6m



579 models are 3.4ha and 21,367m<sup>3</sup>. This comparison demonstrates that horizontal resolution is of paramount  
580 importance when simulating flows through complex topography. It seems that for Cork City centre comprising  
581 of dense network of narrow streets, neither the 5m resolution requirement nor 3 cell street span would resolve  
582 complex flood flow at satisfactory level of accuracy.

583

### 584 **3.5 Flood water velocities**

585 Another significant advantage of MSN\_Flood is its ability to simulate the velocities of flood waters. As oppose  
586 to simplified 2D hydraulic models frequently used in urban flooding, the hydrodynamic MSN\_Flood includes  
587 both the continuity and momentum equations, solving for both water elevations and water velocities. Figure 25  
588 shows an example of flood water velocities computed by MSN\_Flood in a selected area of Cork city centre  
589 blown up for ease of viewing; one can see flood waters in both the river channel and the urban floodplain. This  
590 zone is characterized by fast flowing shallow water subject to rapid transitions as it flows down through the  
591 steep section of recreational grounds adjacent to the river channel. The city downtown, in contrast, is a ponding  
592 area with relatively stagnant waters.

593 Knowledge of velocity fields facilitates better understanding of flood water hydrodynamics and in particular the  
594 mechanisms of flood propagation. The routes and speeds of flood waves provide important information for the  
595 evaluation of flood risks to people's safety and to property, as well as to the planning and actions of emergency  
596 response teams.

597

## 598 **4 Discussion**

599 Inundation of coastal areas due to coastal and/or fluvial urban flooding mechanisms is a very complex  
600 hydrological phenomena, and developing a modelling system to accurately simulate it is not a trivial task. The  
601 research presented in this paper demonstrates that the concept of nesting models is very suitable for complex  
602 urban coastal flooding as they facilitate the development of an integrated system capable of resolving  
603 hydrodynamics at spatial scales commensurate with flows and physical features of the region of interest. The  
604 modelling system adopted here determines physical processes simultaneously at different scales ranging from  
605 bay-size circulation (90 m) through mesoscale processes of coastal waters at 30 m resolution down to the ultra-  
606 high scale environment of 2m. Validation results show that the model performs well at each of these scales.

607 The MSN\_Flood model developed for use in this research is well suited for high resolution urban flood  
608 simulation for a number of reasons. Firstly, it allows smooth transition of the model solution between coastal



609 waters and river floodplains while giving a very high level of conservation of mass and momentum between  
610 parent and child grid (Nash and Hartnett, 2010). Through incorporation of ghost cells and formulation of a  
611 dynamic internal boundary, MSN\_Flood is designed to minimize boundary formulation error and therefore to  
612 transfer mass and momentum across the nested boundary without loss of nested solution accuracy. The  
613 reduction in boundary errors yields also a significant improvement in model stability at the nested boundary and  
614 CG accuracy. This in turn permits stable flooding and drying at the boundary; moreover, these process are  
615 allowed to approach the boundary of the nested domain from either upstream or downstream. The so-called  
616 moving boundary allows then embedding of a child grid model within the parent model in areas where the  
617 nested boundary may wet or dry making the model highly flexible in application. Interestingly, such highly  
618 reduced boundary formulation errors is achieved in a nesting mechanism where the nested boundary comprises  
619 of only two cells of columns or rows (ghost cells and internal boundary cells). For comparison, in many nested  
620 models poor accuracy due to boundary formulation errors is commonly compensated by indirect solutions such  
621 as boundary configuration (e.g. location). For example, Kashefipour et al. (2002) in order to reduce possible  
622 nesting error dynamically link 2D coastal model with 1D river model by using overlapping grids at the  
623 boundary – a common area where boundary values are exchanged between two models. Such model setup is  
624 not required in MSN\_Flood where accurate exchange of boundary conditions occurs along a boundary.

625 Secondly, the model has virtually no limit to the number of specified nesting levels (and spatial resolution) and  
626 is primarily constrained by computational effort rather than numerical stability. The highest resolution of 2 m set  
627 for this study was dictated solely by the resolution of available LiDAR data and higher resolutions are easily  
628 achievable if suitable terrain data is available. For example, a 0.025 m resolution was used to simulate flows  
629 corresponding to those in a physical scale model of a harbour of dimensions 1.0x1.0x0.25 m (Nash and Hartnett  
630 2014). In this way, the model allows improved accuracy of solution when compared to a lower resolution parent  
631 model where the improved accuracy is similar to that of a similar high resolution single grid model but the  
632 computational effort is significantly reduced.

633 Thirdly, the model provides adequate solutions at scales sufficient for processes of interest, such as coarse  
634 resolution coastal circulation and fine resolution flood inundation. This is attributed to the robust hydrodynamic  
635 module which in essence adopts the well-tested numerical scheme and discretisation methods described by  
636 Falconer and Chen (1991). The uniqueness and improvement of MSN\_Flood over other nested models is its  
637 formulation of the nested boundary in the area where flooding and drying may occur. In order to accommodate  
638 flooding and drying of boundary cells the model allows a moving nested boundary so that large sections of the



639 boundary can alternatively wet and dry. The stable flooding and drying of boundary cells results from the  
640 internalisation of the nested boundary combined with an adaptive interpolation technique tailored specifically  
641 for this model. To the author's knowledge the development of a non-continuous moving nested boundary in a  
642 circulation model is novel. Such an innovative solution does not pose restrictions on the location of nested grids  
643 with regards wetting and drying (as demonstrated by the application to Cork Harbour) and, therefore, allows  
644 flexibility of model setup.

645 Finally, in the context of urban flood modelling, MSN\_Flood's ability to simulate horizontal components of  
646 water velocity is a significant advantage over simpler hydraulic models commonly used in flood modelling; the  
647 complexity of urban topography (buildings, vegetation, walls, roads, embankments, ditches etc) necessitates at  
648 least two-dimensional treatment of surface flows (Cook and Merwade, 2009). Spatial and temporal distribution  
649 of velocity fields is also required for assessment of flood risk to people and property associated with a certain  
650 flood flow magnitude. Thus, this feature will greatly benefit flood hazard management.

651 Although the modelling framework seems to be the main factor controlling accuracy of model predictions, other  
652 factors such as model resolution, datasets and model parameterization also play a crucial role. In relation to  
653 model topography/bathymetry, these aspects are interconnected and need to be considered jointly. Comparing  
654 the 6m and 2 m grid models it can be seen that results are quite sensitive to the spatial resolution of the model.  
655 The resolution acts as a filter on the model terrain so the model error increases with decreasing spatial  
656 resolution, as the definition of topographic features (walls, hedges etc) are progressively lost from the model  
657 bathymetry. There is a dual effect of this. Firstly, as the resolution becomes less granular the topographic  
658 complexity of high density small features become sub-grid phenomena which then become parameterised  
659 through roughness coefficients. Spatially varying roughness needs to be specified for different terrains, this is  
660 determined based on surface classification (such as land type, vegetation or roads) within model sensitivity and  
661 calibration. Secondly, the loss of larger objects such as buildings makes the model inherently ill-conditioned and  
662 their loss cannot be remedied through modification of roughness coefficient alone. Errors are additionally  
663 amplified by a presence of bias in the topographic data resulting from LIDAR related post-processing  
664 difficulties such as representation of surface objects discussed in Mason et al. (2003).

665

## 666 **5 Conclusions**

667 In this research, high-resolution multi-scale modelling of coastal flooding due to tides, storm surges and rivers  
668 inflows is performed. A state-of-the-art modelling system, MSN\_Flood, for simulation of coastal flood



669 inundation using dynamic downscaling through a cascade of multiple nested grids, was developed to provide a  
670 methodology for accurate assessment of flood inundation. A comprehensive assessment of the modelling system  
671 was carried out for the coastal city of Cork, which is frequently subject to flooding. A November 2009 extreme  
672 flood event driven by both coastal and fluvial mechanisms was selected as a study case. In its application to  
673 Cork City, the flood model comprises of four dynamically nested grids that resolve the hydrodynamics of Cork  
674 Harbour and Cork City at four different scales: 90m, 30m, 6m and 2m. The urban flood model of 2m horizontal  
675 grid resolution is used to simulate flood water inundation of Cork City.

676 The main findings from this research divided into two thematic groups are summarised here:

677 1. Model computational performance:

678 (a) The nesting model framework allows the model operation at practically any desired horizontal  
679 resolution, including scales commensurate with resolution of LiDAR data making an optimal use of  
680 such datasets. In the current setup, a four-nest cascade telescopes resolution down to the level of  
681 LiDAR resolution which is sufficient to capture small scale flow features.

682 (b) The model has no limits as to the number of nesting levels and the numerical stability is maintained  
683 down to the finest resolution.

684 (c) Computational effort is dictated by the number of nesting levels, the horizontal resolution of each  
685 nested grid and the extents of each nested grid. Nevertheless, at the finest resolution the nested model  
686 was found to be almost as accurate as a single grid model of the same resolution but at 96% saving in  
687 computational cost.

688 (d) Due to its robust flooding and drying routine, the model maintains numerical stability and accuracy in  
689 any part of the model domain affected by these processes.

690 (e) Internalisation of the nested boundary through a use of ghost cells combined with a tailored adaptive  
691 interpolation technique permits flooding and drying of the nested boundary creating highly dynamic  
692 moving boundaries. Moreover, the flooding and drying mechanism can approach the boundary of the  
693 nested domain from either upstream or downstream. Nesting with a moving boundary allows  
694 embedding of a child grid model within the parent model in areas where the nested boundary may wet  
695 or dry. This unique feature of MSN\_Flood provides a high degree of choice regarding the location of  
696 the boundaries to the nested domain and therefore flexibility in model application. This capability gives  
697 MSN\_Flood significant advantages over other models.

698





- 699 2. Model accuracy:
- 700 (f) The modelling system demonstrates a good capability to accurately determine physical processes at
- 701 different spatial scales including mesoscale coastal water circulation (90m) and small scale
- 702 hydrodynamics of complex urban floodplains (2m).
- 703 (g) The extent of flood inundation into floodplains of Cork City and maximum water levels reached during
- 704 flooding were accurately simulated by the urban flood 2 m grid model.
- 705 (h) Fine horizontal resolution is crucial for accurate assessment of inundation. Comparison of 6m and 2m
- 706 grid model  $RE_T$  in water levels shows a noticeable reduction in model performance at coarser resolution
- 707 over the entire domain and the error is generally greater in the dense street network of urbanized zone.
- 708 (i) The urban flood model provides full characteristics of water levels and flow regimes necessary for
- 709 assessment of flood risk to people's safety associated with particular flood water levels and associated
- 710 flood water velocities.

711

712 To conclude, near-unlimited model resolution, geographically unconstrained (due to wetting and drying) nested

713 model setup, robust wetting and drying routine, computational efficiency and the capability to simulate both

714 water elevations and velocity fields, make the MSN\_Flood a valuable tool for studying coastal flood inundation.

715 This research demonstrates that the adopted methodology can be successfully used in applications to coastal

716 flood modelling including complex urban environments. It can provide, at specific instances of time, accurate

717 spatial distributions of water elevations and flow magnitudes in inundated areas and can, thus, provide critical

718 information to assess possible extents of flood inundation, periods of inundation, maximum water elevations

719 reached and flood wave propagation routes and speeds. Ultimately, it can be directly used for evaluation of

720 flood risks to the area and indirectly, through some functional relationships, for risk assessment of human safety

721 and property damage. The methodology explored in this research, when applied in a forecasting sense,

722 constitutes a high resolution flood warning and planning system that can aid local decision makers targeting

723 high flood risk areas.

724

#### 725 **Acknowledgements**

726 This publication has emanated from research conducted with the financial support of Science

727 Foundation Ireland (SFI) under Grant Numbers SFI/12/RC/2302 and SFI/14/ADV/RC3021.

728



729 **References**

- 730 Bates, P.D., Dawson, R.J., Hall, J.W., Horritt, M.S., Nicholls, R.J., Wicks, J., Hassan, M.A.A.M.: Simplified  
731 two-dimensional numerical modelling of coastal flooding and example applications. *Coastal Engineering* 52,  
732 795-810, 2005.
- 733 Bates, P.D., De Roo, A.P.J.: A simple raster-based model for flood inundation simulation. *Journal of Hydrology*  
734 236, 54-77, 2000.
- 735 Bates, P.D., Horritt, M.S., Fewtrell, T.J.: A simple inertia formulation of the shallow water equations for  
736 efficient two-dimensional flood inundation modelling. *Journal of Hydrology* 387, 33-45, 2010.
- 737 Brown, J.D., Spencer, T., Moeller, I.: Modeling storm surge flooding of an urban areas with particular reference  
738 to modelling uncertainties; A case study of Canvey Island, United Kingdom. *Water Resources research* 43,  
739 W06402, 2007.
- 740 Chen, X.: Dynamic coupling of a three-dimensional hydrodynamic mode with a latterly averaged, two-  
741 dimensional hydrodynamic model. *Journal of Geophysical Research* 112, C07022, 2007.
- 742 Cook, A., Merwade, V.: Effect of topographic data, geometric configuration and modelling approach on flood  
743 inundation mapping. *Journal of Hydrology* 377, 131-142, 2009.
- 744 DHI Software, 2001. Mike 21 flow model: hydrodynamic module user guide. DHI water and Environment.
- 745 Falconer, R.A.: A mathematical model study of the flushing characteristics of a shallow tidal bay. *Proc Inst*  
746 *Civil Eng 2 Res and Theory* 77, 311-332, 1984.
- 747 Falconer, R.A., Chen, Y.P.: An improved representation of flooding and drying and wind stress effects in a 2-D  
748 tidal numerical model. *Proc Inst Civil Eng 2 res and Theory* 91, 659-678, 1991.
- 749 Fewtrell, T.J., Duncan, A., Sampson, C.C., Neal, J.C., Bates, P.D.: Benchmarking urban flood models of  
750 varying complexity and scale using high resolution terrestrial LiDAR data. *Physics and Chemistry of the Earth*  
751 36, 281-291, 2011.
- 752 Formaggia, L., Gerbeau, J.F., Nobile, F., Quarteroni A.: On the coupling of 3D and 1D Navier-Stokes equations  
753 for flow problems in compliant vessels. *Comput Methods Appl Mech Eng* 191, 561-582, 2001.
- 754 Gallegos, H.A., Schubert, J.E., Sanders, B.F.: Two-dimensional high-resolution modelling of urban dam-break  
755 flooding: A case study of Baldwin Hill, California. *Advances in Water Resources* 32, 1323-1335, 2009.
- 756 Gomes-Pereira, L.M., Wicherson, R.J.: Suitability of laser data for deriving geographical data: a case study in  
757 the context of management of fluvial zones. *Photogrammetry and Remote Sensing* 54, 105-114, 1999.



- 758 Haidvogel, D.B., H. Arango, W.P. Budgell, B.D. Cornuelle, E. Curchitser, E. Di Lorenzo, K. Fennel, W.R.  
759 Geyer, A.J. Hermann, L. Lanerolle, J. Levin, J.C. McWilliams, A.J. Miller, A.M. Moore, T.M. Powell, A.F.  
760 Shchepetkin, C.R. Sherwood, R.P. Signell, J.C. Warner, J. Wilkin: Ocean forecasting in terrain-following  
761 coordinates: Formulation and skill assessment of the Regional Ocean Modeling System. *J. Comp. Phys.* 227(7),  
762 3595-3624, 2008.
- 763 Halcrow: Lee catchment flood risk assessment and management study. Hydrology report. Halcrow Group  
764 Ireland Ltd. , 2008.
- 765 Holt, J., Harle, K, Proctor, R., Michel, S., Ashworth, M., Batstone, C., Allem, I., Holems, R., Smyth T., Haines,  
766 K., Bretherton, D., Smith G.: Modelling the global coastal ocean. *Philos Trans Soc A* 367, 939-951, 2009.
- 767 Horritt, M.S.: Calibration and validation of a 2-dimensional finite element flood flow model using satellite radar  
768 imagery. *Water Resources Research* 36, 3279-3291, 2000.
- 769 Horritt, M.S., Bates, P.D., Mattinson, M.J.: Effects of mesh resolution and topographic representation in 2D  
770 finite volume models of shallow water fluvial flow. *Journal of Hydrology* 329, 306-314, 2006.
- 771 Hunter, N.M., Bates, P.D., Neelz, S., Pender, G., Villanueva, I., Wright, N.G., Liang, D., Falconer, R.A., Lin,  
772 B., Waller, S., Crossley, A.J., Mason, D.C.: Benchmarking 2D hydraulic models for urban flooding. *Water*  
773 *Management* 161, 13-30, 2008.
- 774 Kashefipour, S.M., Lin, B., Harris, E., Falconer, R.A.: Hydro-environmental modelling for bathing water  
775 compliance of an estuarine basin. *Water Research* 36, 1854-1868, 2002.
- 776 Korres, G., Lascaratos, A.: A one-way nested eddy resolving model of the Aegean and Levantine Basins:  
777 implementation and climatological runs. *Ann Geophys* 21, 205-220, 2003.
- 778 Lin, B., Falconer, R.A.: Tidal flow and transport modelling using ULTIMATE QUICKEST scheme. *Journal of*  
779 *hydraulic Engineering* 123, 303-314, 1997
- 780 McMillian, H.K., Brasington, J.: Reduced complexity strategies for modelling urban floodplan inundation.  
781 *Geomorphology* 90, 226-243, 2007.
- 782 Mark, O., Weesakul, S., Apirumanekul, C., Aroonnet S.B., Djordjevic, S.: Potentials and limitations of 1D  
783 modelling of urban flooding. *Journal of Hydrology* 299, 284-299, 2004.
- 784 Marks, K., Bates, P.D.: Integration of high-resolution topographic data with floodplain flow models.  
785 *Hydrological processes* 14, 2109-2122, 2000.



- 786 Mason, D.C., Cobby, D.M., Horritt, M.S., Bates, P.D.: Floodplain friction parameterization in two-dimensional  
787 river flood models using vegetation heights derived from airborne scanning altimetry. |Hydrological Processes  
788 17, 1711-1732, 2003.
- 789 Mason, D.C., Horritt, M.S., Hunter, N.M., Bates, P.D.: Use of fused airborne scanning laser altimetry and digital  
790 map data for urban flood modelling. Hydrological Process 21, 1436-1447, 2007.
- 791 Nash, S.: Development of an adaptive mesh inter-tidal circulation model. PhD Thesis Collage of Engineering  
792 and Informatics, National University of Ireland, Galway, 2010.
- 793 Nash, S., Hartnett, M.: nested circulation modelling of inter-tidal zones: details of nesting approach  
794 incorporating moving boundary. Ocean Dynamics 60, 1479-1495, 2010.
- 795 Nash, S., Hartnett, M.: Development of a nested circulation model: boundary error reduction. Environmental  
796 Modelling and Software 53, 65-80, 2014.
- 797 Nittis, K., Perivoliotis, L., Korrea G., Tziavos, C., Thanos, I.: Operational monitoring and forecasting for marine  
798 environmental applications in the Aegean sea. Environ Modell Softw 21, 243-257, 2006.
- 799 Olbert A.I., Hartnett M.: Storms and surges in Irish coastal waters. Ocean Modelling 34, 50–62, 2010.
- 800 Pappenberger, F., Beven, K., Horritt, M., Blazkova, S.: Uncertainty in the calibration of effective roughness  
801 parameters in HEC-RAS using inundation and downstream level observations. Journal of Hydrology 302, 46-  
802 69, 2005.
- 803 Pender, G., Neelz, S.: Benchmarking of 2D hydraulic modelling packages. SC080035/R2 Environmental  
804 Agency, Bristol, p. 169, 2010.
- 805 Ponte, R.M.: Understanding the relation between wind- and pressure-driven sea level variability. Journal of  
806 Geophysical Research 99, 8033-8039, 1994.
- 807 Robins, P.E., Davies, A.G., Jones, R.: Application of coastal model to simulate present and future inundation and  
808 aid coastal management. J Coast Conserv 15, 1-14, 2011.
- 809 Sanders, B.F., Schubert, J.E., Detwiler, R.L.: ParBreZo: A parallel, unstructured grid, Godunov-type, Shallow  
810 water code for high-resolution flood inundation modelling at the regional scale. Advances in Water Resources  
811 33, 1456-1467, 2010.
- 812 Simmons A.J., Burridge D.M., Jarraud M., Girard C., Wergen W.: The ECMWF medium-range prediction  
813 models development of the numerical formulations and the impact of increased resolution. Meteorol Atmos  
814 Phys 40, 28-6, 1989.



815 Smith, L.C.: Emerging applications of interferometric synthetic aperture radar (INSAR) in geomorphology and  
816 hydrology. *Annals Assoc Am Geography* 92, 385-398, 2002.

817 Uppala, S.M., Kallberg, P.M., Simmons, A.J., Andrae, U., Bechtold, V., Fiorino, M., Gibson, J., Haseler, J.,  
818 Hernandez, A., Kelly, G., Li X., Onogi, K., Saarinen, S., Sokka, N., Allan, R., Andersson, E., Arpe, K.,  
819 Balmaseda, M., Beljaars, A., Berg, L., Bidlot, J., Bormann, N., Caires, S., Dethof, A., Dragosavac, M., Fisher,  
820 M., Fuentes, M., Hagemann, S., Holm, E., Hoskins, B., Isaksen, L., Janssen, P., McNally, A., Mahfouf, J.,  
821 Jenne, R., Morcrette, J., Rayner, N., Saunders, R., Simon, P., Sterl, A., Trenberth, K., Untch, A., Vasiljevic ,D.,  
822 Viterbo, P., Woollen, J.: The ERA-40 reanalysis. *Quart J Roy Meteorol Soc* 131, 2961-3012, 2005.

823 Yang, Z., Wang, T., Khangaonkar, T., Breithaupt, S.: Integrated modelling of flood flows and tidal  
824 hydrodynamics over coastal floodplains. *Environmental Fluid Mechanics* 12, 63-80, 2012.

825 Yu, D., Lane, S.N.: Urban fluvial flood modelling using two-dimensional diffusion-wave treatment: 1. Mesh  
826 resolution effects. *Hydrological Processes* 20, 1541-1565, 2006.

827  
828  
829  
830  
831  
832  
833  
834  
835  
836  
837  
838  
839  
840  
841  
842  
843



844 Tables

845

846 Table 1. Configuration of nested models

| Model               | Grid size<br>m | Timestep<br>s | Parent model | Parent-to-model<br>grid ratio |
|---------------------|----------------|---------------|--------------|-------------------------------|
| Parent grid (PG90)  | 90             | 18            | --           | 1:1                           |
| Single grid (SG30)  | 30             | 6             | PG90         | 1:1                           |
| Child grid 1 (CG30) | 30             | 6             | PG90         | 3:1                           |
| Child grid 2 (CG06) | 6              | 0.6           | CG30         | 5:1                           |
| Child grid 3 (CG02) | 2              | 0.2           | CG06         | 3:1                           |
| Single grid (SG02)  | 2              | 0.2           | CG06         | 1:1                           |

847

848

849 Table 2. Summary of error analyses for PG90 and CG30 models within CG30 model area.

| Error<br>Parameter               | Analyses | SG30 |      |
|----------------------------------|----------|------|------|
|                                  |          | PG90 | CG30 |
| Water Elevation:                 |          |      |      |
| - $RE_D$ [%]                     |          | 5.9  | 1.1  |
| - $AE_D$ [ $\times 10^{-2}$ m]   |          | 8.0  | 1.2  |
| - $RE_T > 1\%$ [%]               |          | 94   | 28   |
| Current Velocity:                |          |      |      |
| - $RE_D$ [%]                     |          | 22.4 | 0.5  |
| - $AE_D$ [ $\times 10^{-3}$ m/s] |          | 2.70 | 0.13 |
| - $RE_T > 5\%$ [%]               |          | 72   | 4    |

850

851

852



853 Table 3. Error statistics of water elevations simulated by the CG06 model and measured at Tivoli tidal gauge  
854 station. Heights are in meters

| Code   | COR   | NSD   | RMSD  | RMSE  | RMSdiff |
|--------|-------|-------|-------|-------|---------|
| CG06_1 | 0.992 | 1.021 | 0.141 | 0.142 | 0.022   |
| CG06_2 | 0.996 | 1.023 | 0.104 | 0.106 | 0.024   |
| CG06_3 | 0.995 | 1.084 | 0.075 | 0.075 | 0.020   |

855

856

857 Table 4. Error statistics of water elevations at four locations simulated by the CG06 and CG02 models. Heights  
858 are in meters

| Code   | COR   | NSD   | RMSD  | RMSE  | RMSdiff |
|--------|-------|-------|-------|-------|---------|
| CG02_1 | 0.995 | 1.033 | 0.080 | 0.111 | -0.081  |
| CG02_2 | 0.997 | 1.014 | 0.109 | 0.195 | -0.181  |
| CG02_3 | 0.998 | 1.045 | 0.056 | 0.076 | -0.064  |
| CG02_4 | 0.999 | 0.999 | 0.006 | 0.006 | 0.000   |

859

860

861

862

863

864

865

866

867

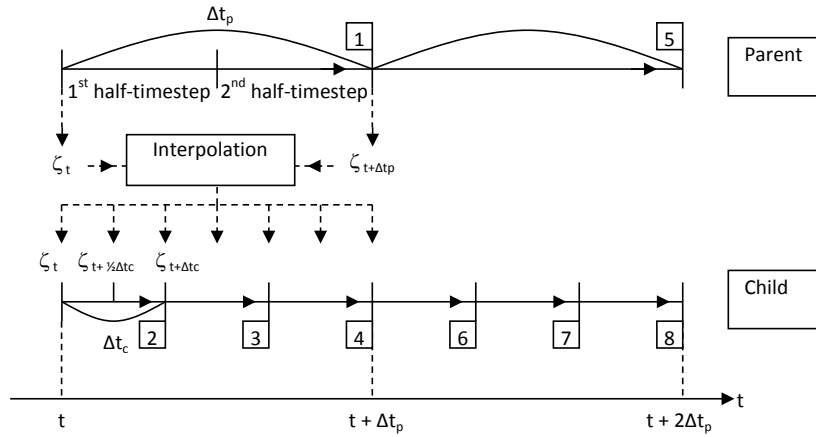
868

869



870 Figures

871

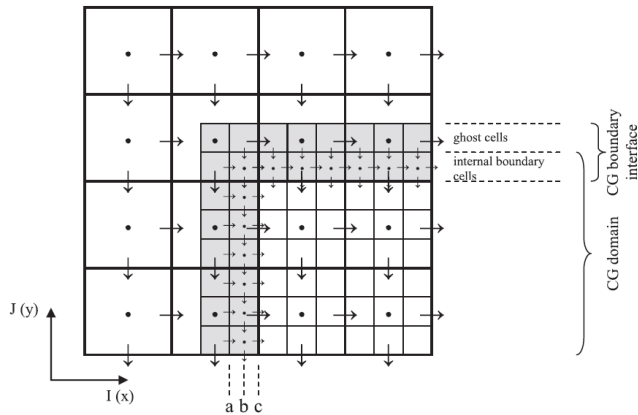


872

873 Figure 1: The nesting procedure for a single level of nesting and one variable only - water surface elevation,  $\zeta$ .

874

875

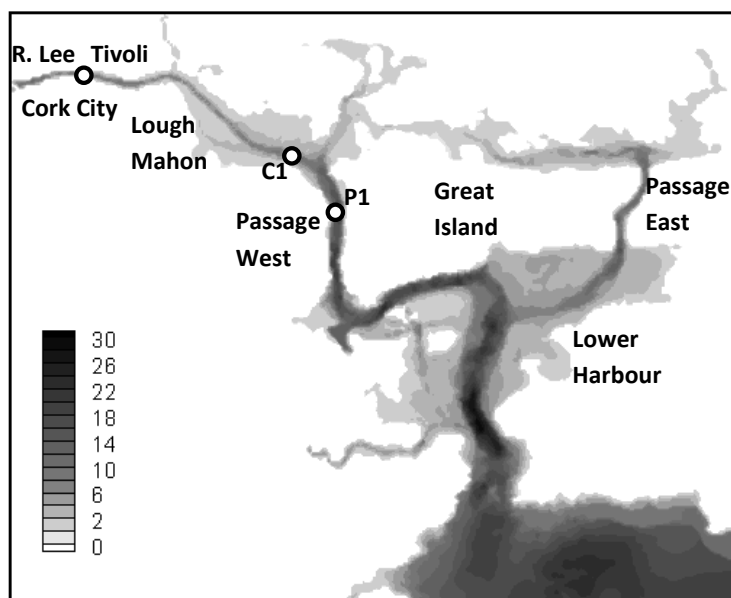


876

877 Figure 2: Schematic illustration of the internal boundary configuration for 3:1 nesting ratio.

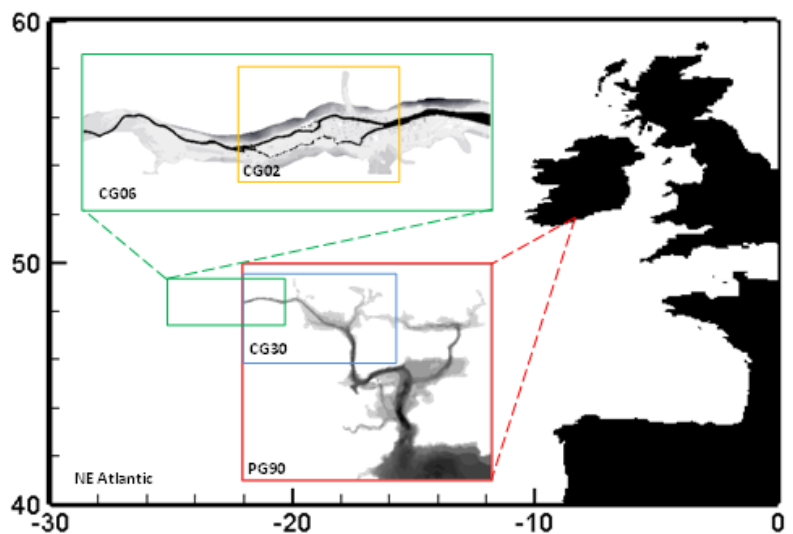
878





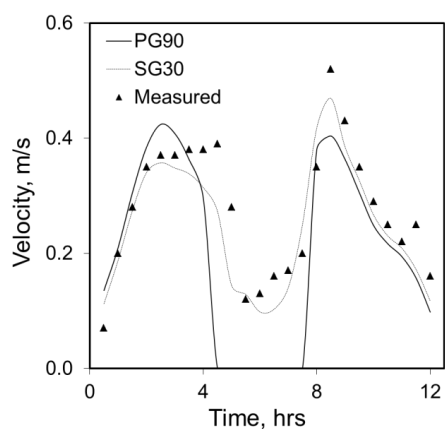
879  
880 Figure 3: Map of Cork Harbour with selected locations.

881



882  
883 Figure 4: Four-level nesting structure of Cork Harbour and City nested model.

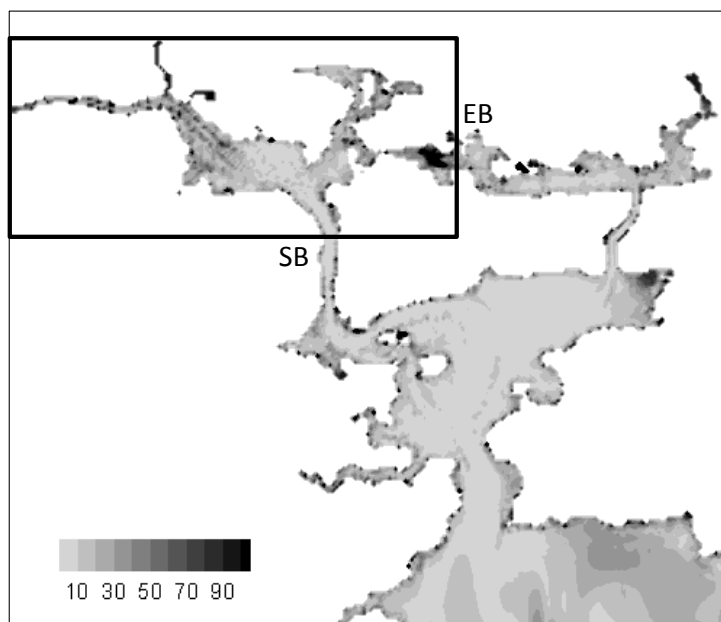
884



885

886 Figure 5: Comparison of computed and measured velocities at Passage West (point C1 in Figure 3).

887



888

889 Figure 6:  $RE_T$  (%) in PG90 velocities. Black box shows extents of CG30 model and locations of nested  
890 boundaries. EB - east boundary, SB – south boundary.

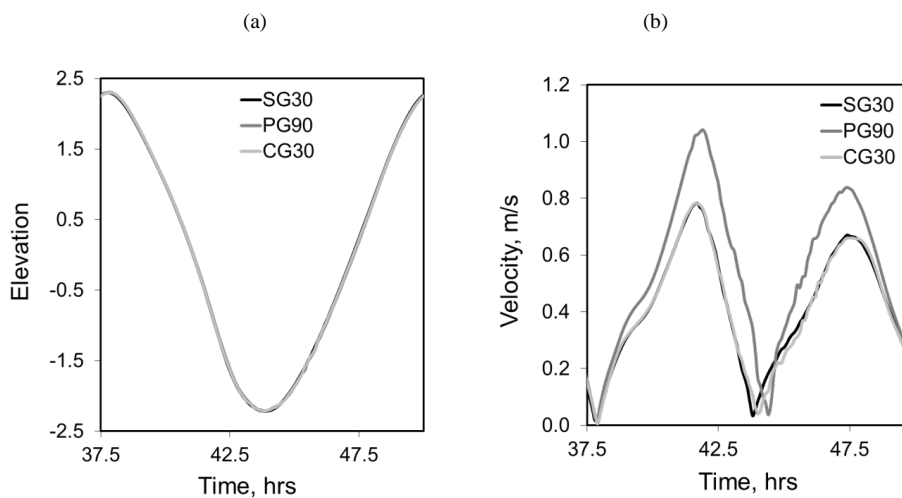
891

892

893



894

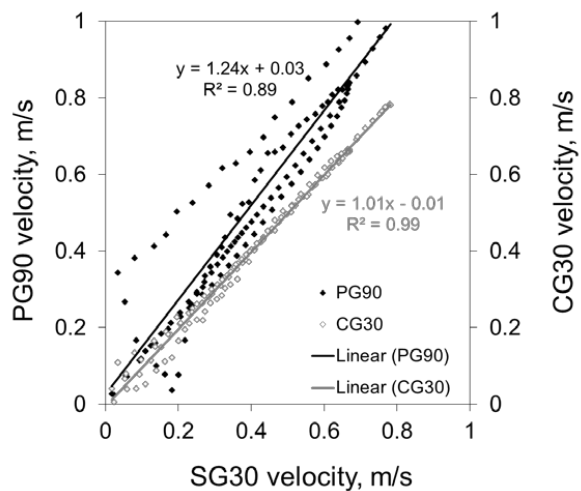


895

896 Figure7: Comparison of (a) water elevations and (b) current velocities at point C1 in Lough Mahon.

897

898



899

900 Figure 8: Comparison of modelled velocities for various grid setups at point C1 in Lough Mahon. Time series  
 901 data are overlain by a linear trend.

902

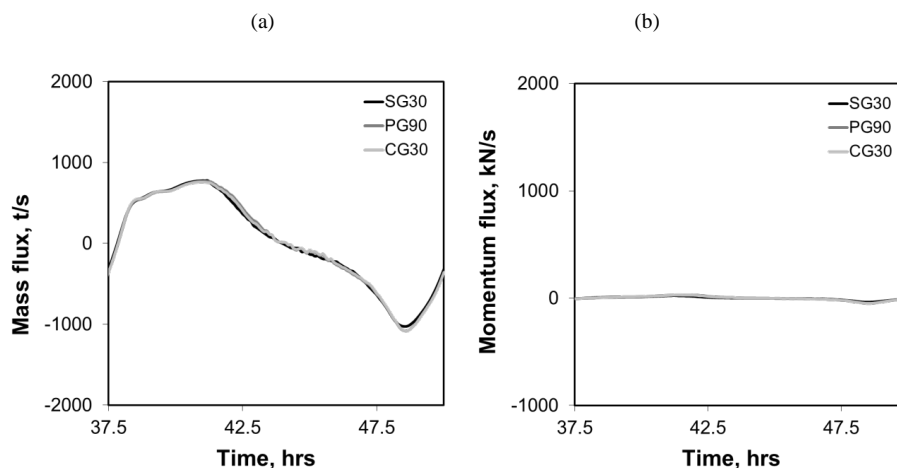
903

904

905



906



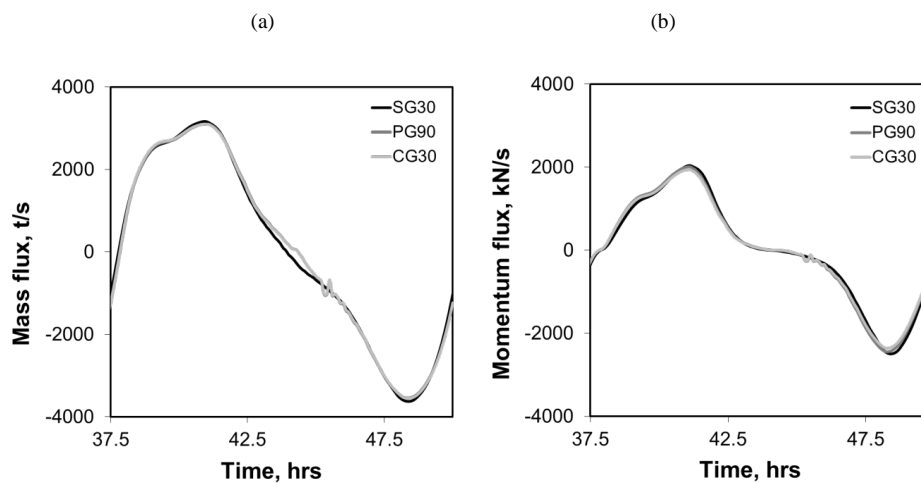
907

908 Figure 9: Comparison of (a) mass and (b) momentum fluxes across EB boundary; PG90 and CG30 timeseries

909 are coincident.

910

911

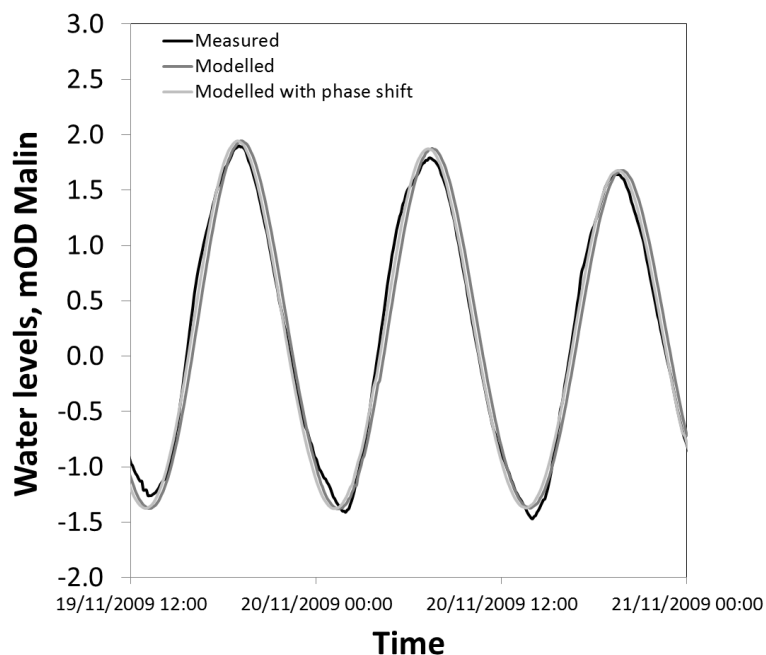


912

913 Figure 10: Comparison of (a) mass and (b) momentum fluxes across SB boundary; PG90 and CG30 timeseries

914 are coincident.

915

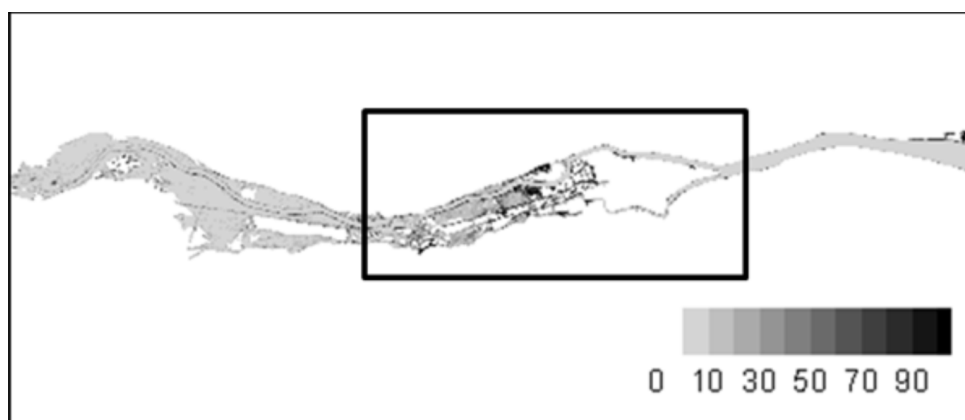


916

917 Figure 11: Water elevations predicted by the CG06 model and measured at Tivoli tidal gauge station.

918

919



920

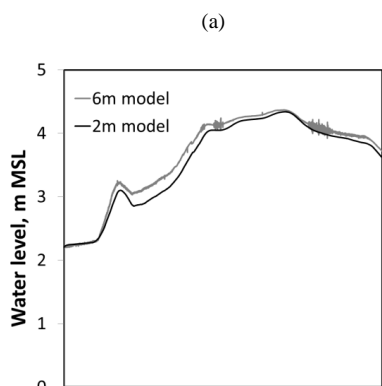
921 Figure 12: Water level  $RE_T$  (%) in CG06 relative to SG02 . Black box shows extents of CG02 model and  
922 locations of nested boundaries.

923

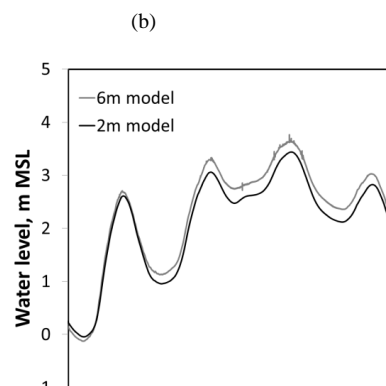
924



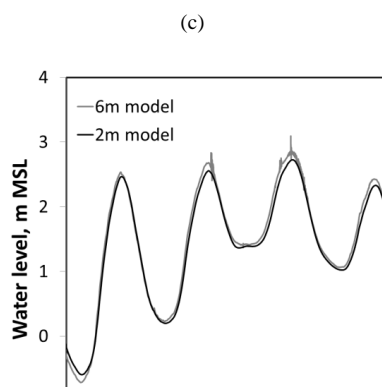
925



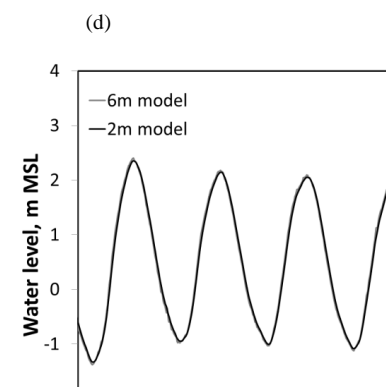
926



927



928

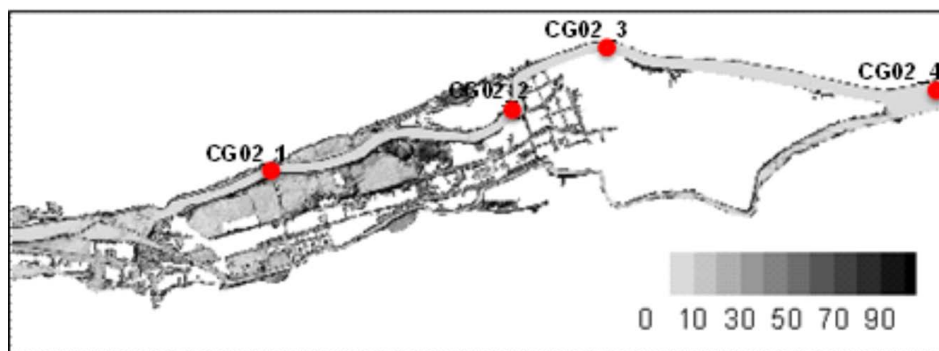


929 Figure 13: Timeseries of water elevations predicted by CG06 and CG02 models at four locations (a) CG02\_1,

930 (b) CG02\_2, (c) CG02\_3, (d) CG02\_4.

931

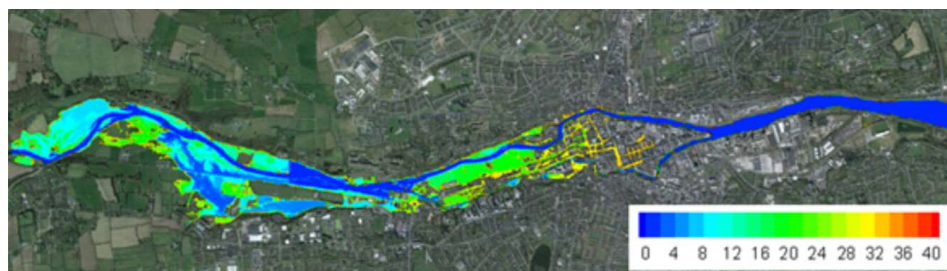
932



933

934 Figure 14: Water level  $RE_T$  (%) in CG02 relative to SG02 . Red dots denotes points used in water level analysis  
935 (see Figure 13).

936



937

938 Figure 15: Temporal evolution of flood wave through upper and lower floodplain of Cork City during  
939 November 2009 flood event modelled by CGO6; contours represent 2-hour intervals.

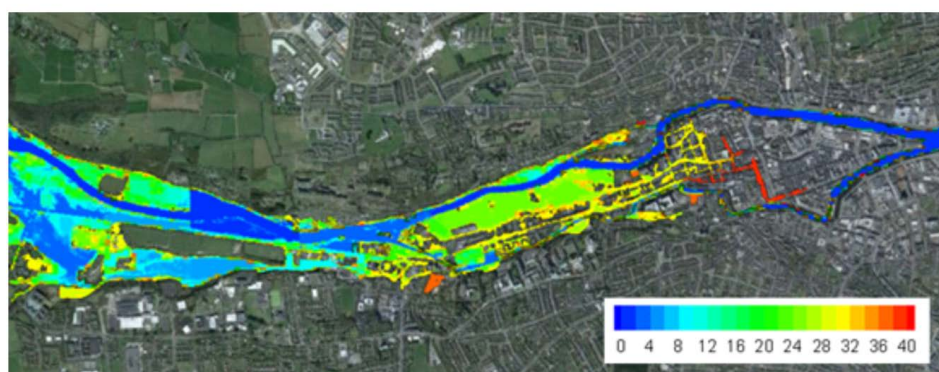
940



(a)



(b)

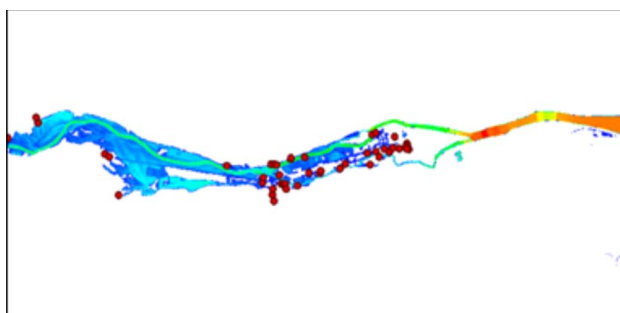


941

942 Figure 16: Maps of flood inundation observed by (a) OPW and (b) modelled (contours represent 2-hour

943 intervals). Evolution of modelled flood wave is a combined output of CG06 and CG02 models.

944



945

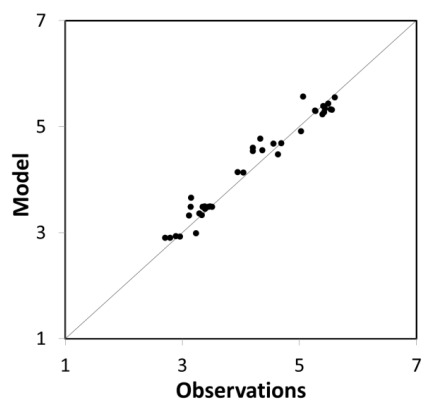
946 Figure 17: Maximum water levels during November 2009 flood event and water level survey points marked as

947 red dots.





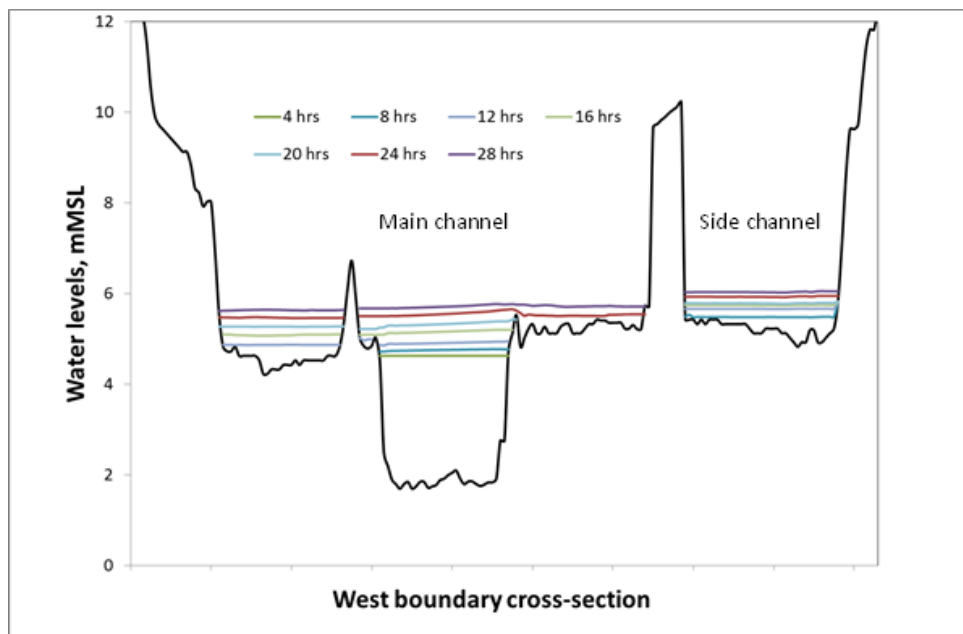
948



949

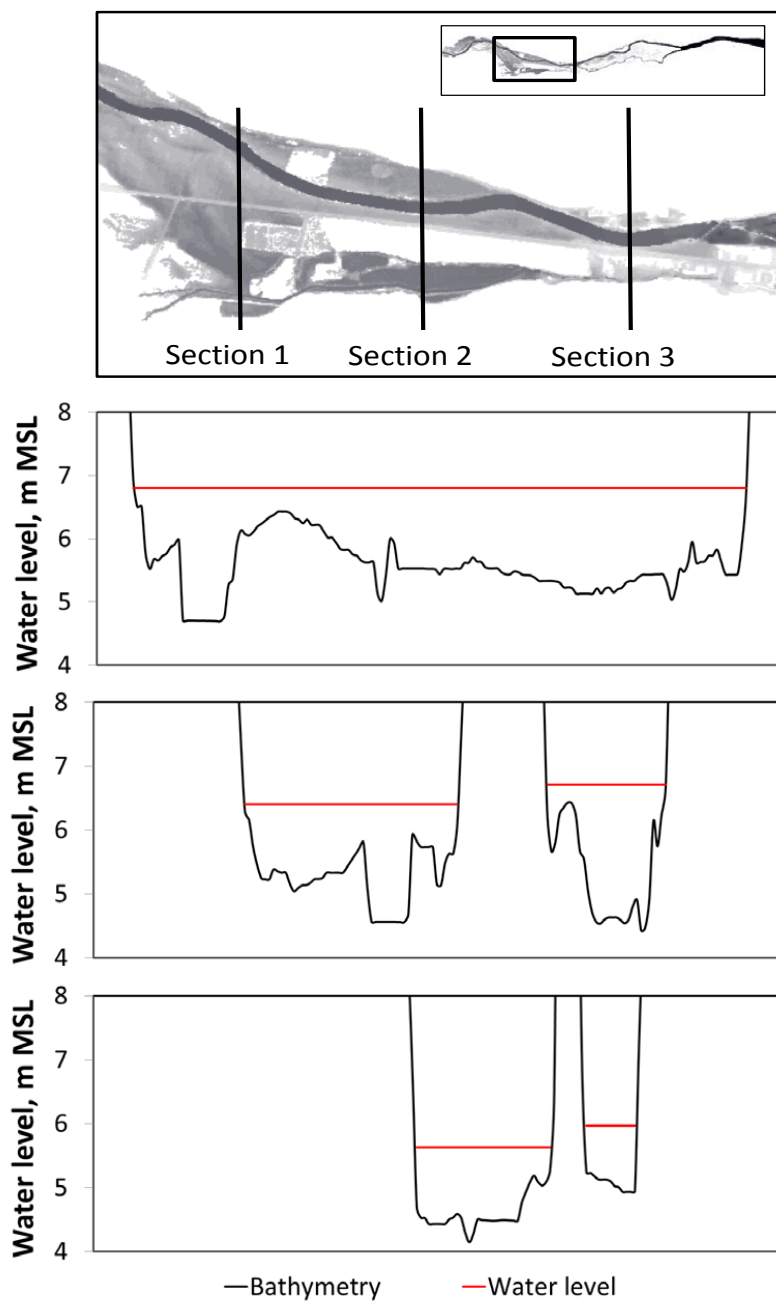
950 Figure 18: Comparison of modelled and observed maximum water elevations at 38 stations.

951



952

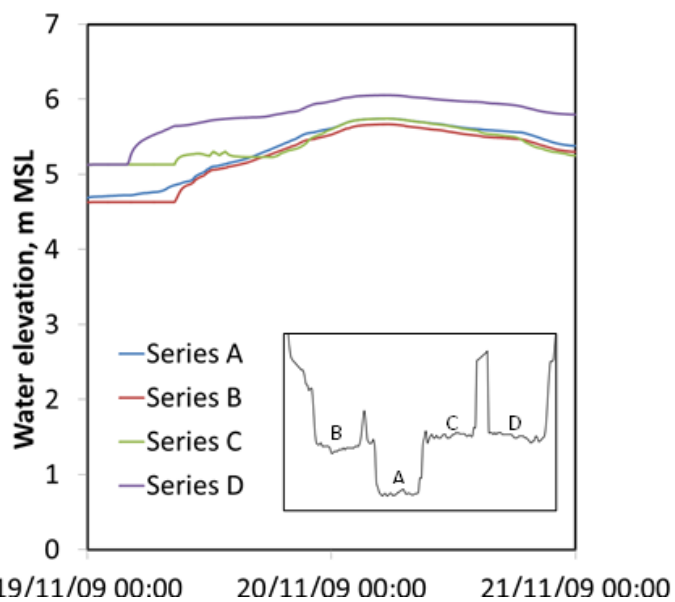
953 Figure 19: Cross section through west boundary of CG02 model with water elevation marks for selected time  
954 points.



955

956 Figure 20: Water elevations at three cross-sections during flooding simulated by CG06.

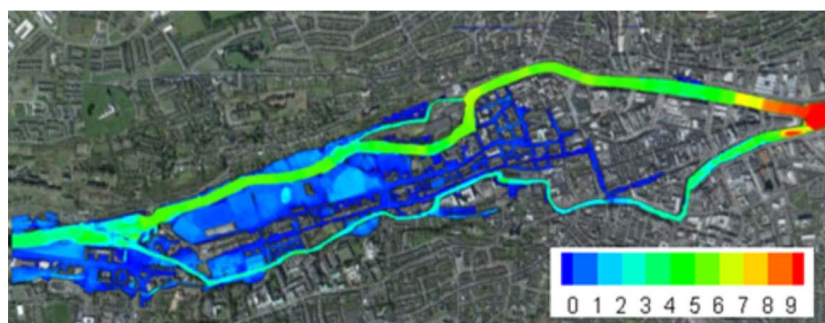
957



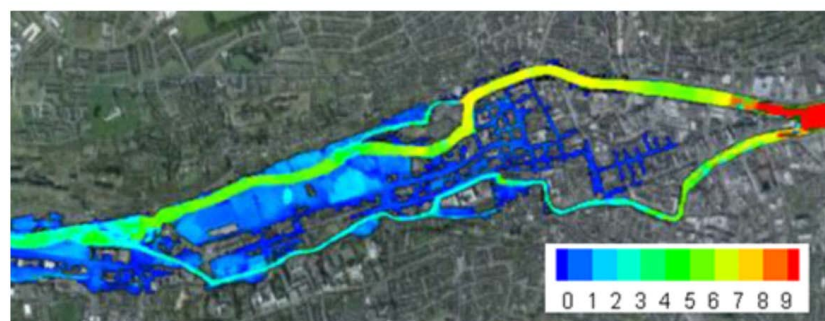
958 19/11/09 00:00 20/11/09 00:00 21/11/09 00:00  
959  
960 Figure 21: Timeseries of water elevations across the western nested boundary of CG02.  
961



(a)



(b)



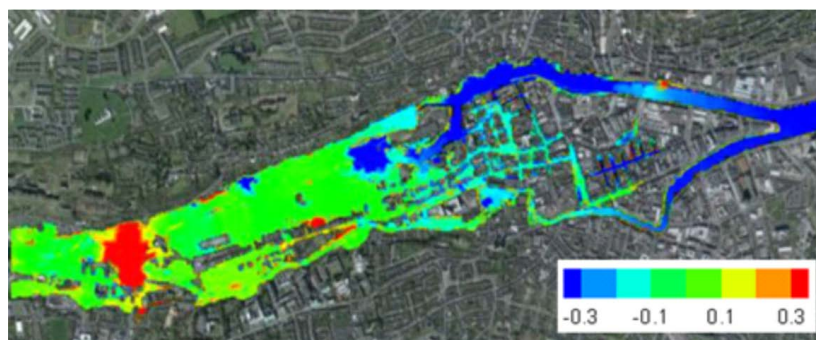
962

963 Figure 22: Comparison of flood extent simulated by (a) CG02 and (b) CG06 models. Contours represent water  
964 levels (m).

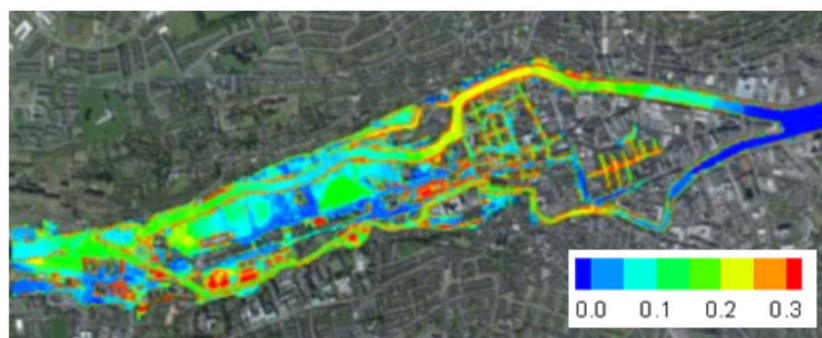
965



(a)



(b)



966

967 Figure 23: (a) Difference in water elevations (m) between CG06 and CG02 models and (b) RMSE contour plot  
968 over time.

969

970

971

972

973

974

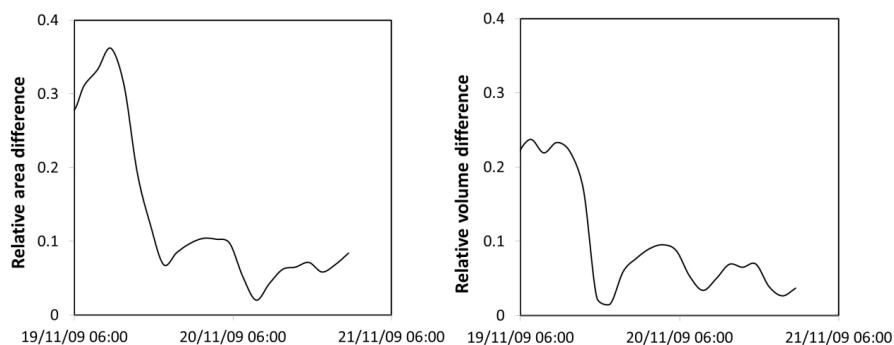
975



976

(a)

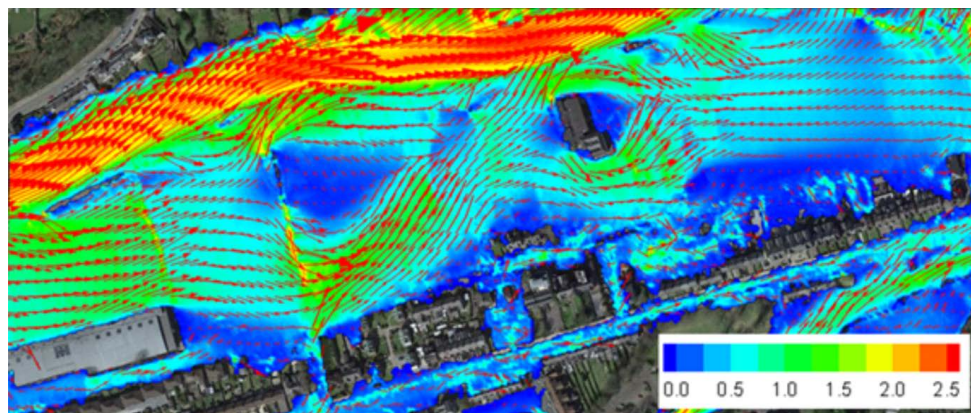
(b)



977

978 Figure 24: Evolution of the relative difference in (a) total area of inundation and (b) volume of water in  
979 inundated area between CG06 and CG02 models. See text for explanation of relative difference.

980



981

982 Figure 25: Map of velocity contours (m/s) with vectors showing magnitude and direction of velocities in the  
983 downstream floodplains of Cork City.

984

985